Utrecht University

Faculty of Earth Sciences

MSc Thesis

Placing further geochemical constraints on the genesis of the Gamsberg Zinc Deposit, Namaqualand Metamorphic Province, South Africa using sulphur isotope data

Author:
Wouter H.M. Roesink
(4094891)

Supervisors:
Prof. Dr. Paul Mason
Dr. Harilaos Tsikos

July 12, 2018

Abstract

The 1.6-2.0Ga Gamsberg deposit is a >200 Mt zinc reserve located in the Aggeneys-Gamsberg mining district in the Northern Cape Province of South Africa, which is host to a cluster of world-class base metal deposits. These four proximal SEDEX-type deposits were formed in an extensional basin, in which Gamsberg occupies the eastern side of the district. The Gamsberg deposit is characterized by an anomalous enrichment in manganese, which greatly complicates ore refinement. Previous work has shown a high abundance and variability of Mn in sphalerite minerals throughout the stratigraphy at the West orebody of Gamsberg. This study goes beyond previous work by determining for the first time sulfur isotope ratio variability in individual sphalerite and iron sulfide minerals with stratigraphic position through the deposit. LA-ICP-MS analysis of the Fe-sulfide- and sphalerite minerals in the samples from the West orebody revealed initially low δ^{34}S values around 0‰ that increased abruptly to high δ^{34}S values of up to +40‰ relative to Vienna Canyon Diablo Troilite (VCDT). This was interpreted as the source of reduced sulfur for initial mineralization being decoupled from the source of reduced sulfur after initial mineralization, thermochemcial reduction of seawater derived sulfate. The strongly positive δ^{34}S values were interpreted as the result of Gamsberg developing later than the other Aggeneys deposits in the closed depositional basin. Manganese variability is interpreted as a finite sediment enrichment as a distal expression of the other Aggeneys SEDEX deposits which was remobilized and progressively depleted during the formation of the Gamsberg deposit. Metamorphism and associated metasomatism during the Namaquan orogeny (1.06-1.03 Ga) were interpreted as a mechanism for introducing secondary sulfide minerals to ore units with an oxidized primary mineral assemblage and mobilizing manganese for incorporation in metamorphic gangue minerals.

Table of Contents

List of Figures

List of Tables

1 Introduction

1.1 The Aggeneys-Gamsberg mining district

The Aggeneys-Gamsberg mining district comprises a cluster of four major stratiform sulfide Cu-Pb-Zn-Ag ore deposits, as well as many lesser base metal deposits, and is located in the Northern Cape Province, South Africa, approximately 600km North North-west of Cape Town. These major deposits, which lay within a 30 km distance, are typical examples of Broken Hill-type (BHT) deposits and include: Swartberg, Broken Hill, which is sometimes further subdivided in Broken Hill and the Broken Hill Deeps; Big Syncline and Gamsberg. These deposits are hosted by amphibolite facies metasedimentary rocks of the Proterozoic (1.6-2.0 Ga) Bushmanland Group (*Reid et al., 1987; McClung et al., 2007; Cornell et al., 2009*). Between them, these deposits contain an estimated 439 Mt of ore at 3.60% Zn, 1.43% Pb, 0.21% Cu and 21ppm Ag (*McClung et al., 2007*). Classified as a low grade, high tonnage deposit, supergiant sediment-hosted Zn-Pb deposit, with a tonnage of 214Mt at 6-6.5% Zn, the Gamsberg deposit is located on the eastern part of the Aggeneys-Gamsberg mining district (Figure 1; *Stalder & Rozendaal, 2004; Vedanta Zinc International*).

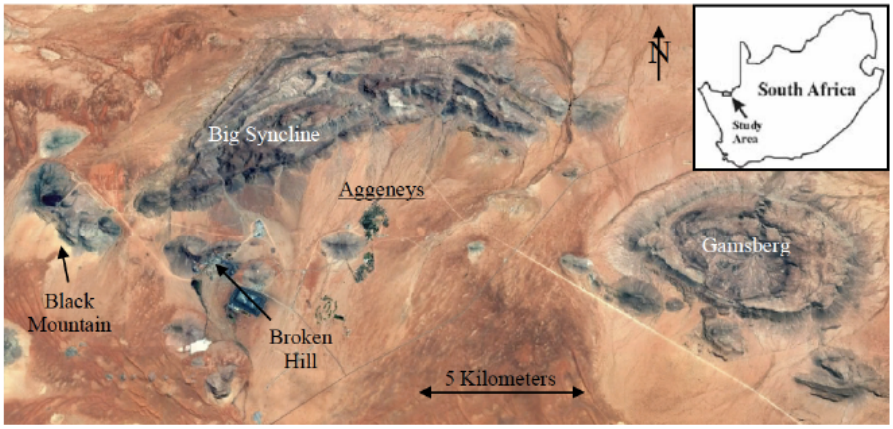

Figure 1: Satellite view of the Aggeneys-Gamsberg Mining District. The deposits are localized in the dark inselbergs contrasting with the surrounding red sandy plane (from Poignant-Molina (2017)).

Intensive exploration activities in the area that have taken place ever since the first economic discovery in the district by R.G. Niemoller at Gamsberg, in the form of a manganiferous iron ore deposit in 1954, and subsequent copper and zinc discoveries in the Prieska area in 1968; have led to the discovery of a substantial 93.5Mt sulfide Zn-Pb ore deposit at Gamsberg in 1973. Exploitation of this supergiant deposit, however, has been problematic up until recent years due to the low zinc grade of the ore and the high manganese content making the ore more difficult and costly to process and refine (*Stalder & Rozendaal, 2004; Schouwstra et al., 2010; McClung & Viljoen, 2011*).

In the typical refinement process that is used to extract metallic zinc from sphalerite (ZnS), zinc is recovered by means of flotation using copper sulphate as an activator. In this process copper replaces the zinc in the lattice of the sphalerite crystal surfaces. This provides sites for xanthate adsorption, which renders the mineral grain hydrophobic. It is then possible to seperate the newly hydrophobic grains from the rest of the ore by means of froth flotation (*Schouwstra et al., 2010*). In the Gamsberg zinc deposit manganese can be found in a number of carrier minerals including some FeMn-silicates, the garnet types spessartine and almandine and alabandite (MnS), as well as the sphalerite lattice (*Stalder & Rozendaal, 2004; Schouwstra et al., 2010; Poignant-Molina, 2017*). *Schouwstra et al (2010)* found that the flotation concentrate contained significant amounts of alabandite, and upon further investigation showed that there was a much higher copper surface coverage on alabandite minerals than on sphalerite grains in pelitic + alabandite ore, concluding that copper is preferentially adsorbed on alabandite mineral surfaces rather than sphalerite. The presence of alabandite is thus extremely detrimental to zinc recovery by sphalerite flotation as it increases the amount of manganese in the final zinc concentrate.

1.2 Aims of the study

Whilst the detrimental effects of the high manganese content in the Gamsberg zinc deposit are well understood (*Schouwstra et al., 2010*), the continuity of- and the controls on the manganese distribution in this deposit are not well characterized. A previous geochemical study on the controls and continuity of the manganese in sphalerite in the North orebody of the Gamsberg zinc deposit, commissioned by Vedanta Resource Limited, produced a single distribution profile from drillhole GAM107, which has been adapted by *Poignant-Molina (2017)* to more accurately represent the raw data from which it was originally constructed (Figure 2).

As a follow-up to the study by Vedanta Resource Limited, *Poignant-Molina (2017)* analyzed 34 samples from drillhole GVD038, which is located in the West orebody (Figure 4). These samples represented homogeneous sphalerite-rich zones throughout 25m of the Gams formation. Geochemical analysis on these samples was carried out by means of an Electron Microprobe (EMP), and resulted in multiple distribution profiles (Figure 3).
From these results *Poignant-Molina* concluded that the sphalerite grains in the Gamsberg ore deposit are in most cases enriched in iron and manganese. The enrichment of Mn+Fe in sphalerites is localized in the lower units of the Gams Formation (A3-B2) and becomes progressively depleted from unit C1 upwards. These signals were interpreted as a shift in basin conditions which caused other primary mineral phases to take up Mn and Fe as trivalent species, causing limited substitution of Mn^{2+} and Fe^{2+} in sphalerite.

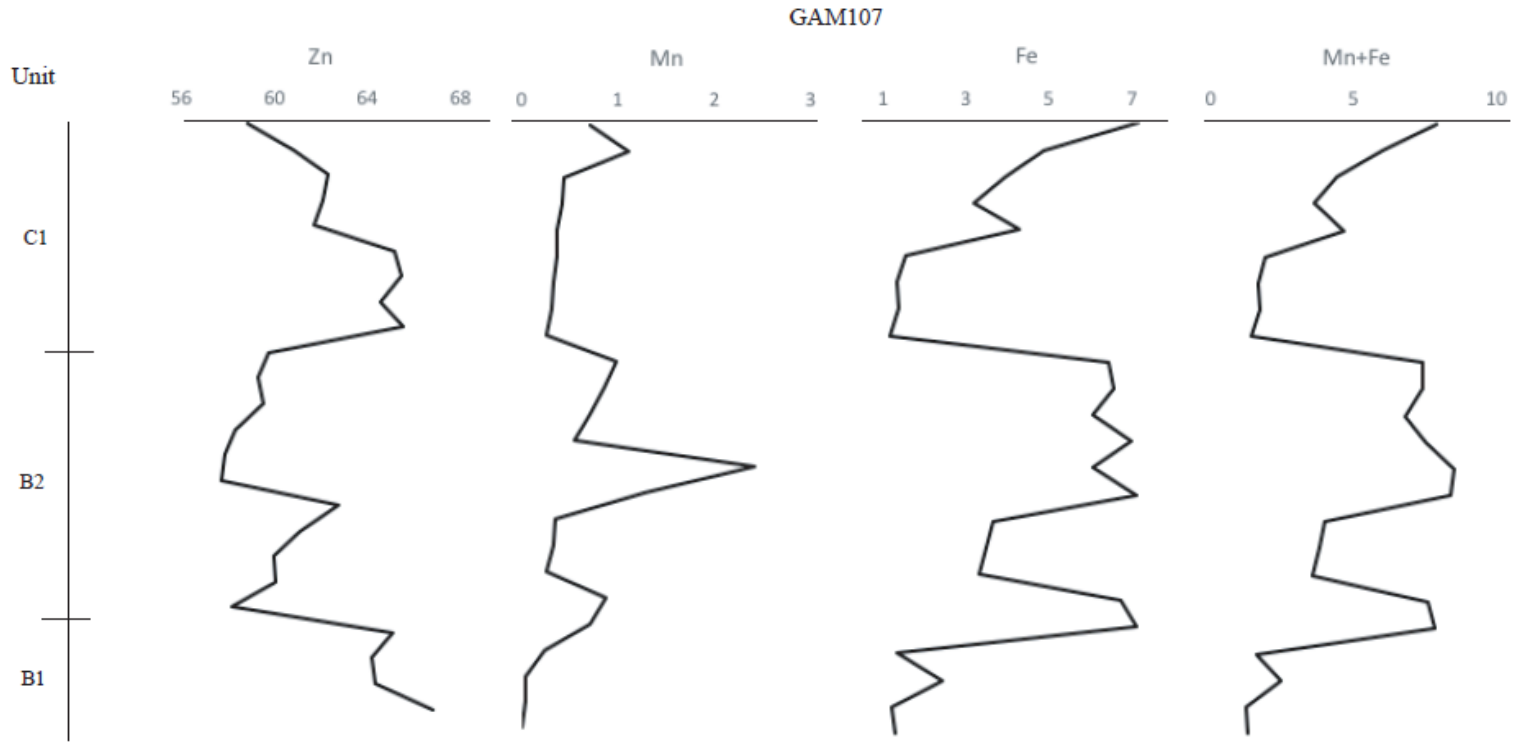

Figure 2: Sphalerite geochemical distribution profiles of Zn, Mn and Fe for drillhole GAM107 against its simplified stratigraphy (from Poignant-Molina (2017)).

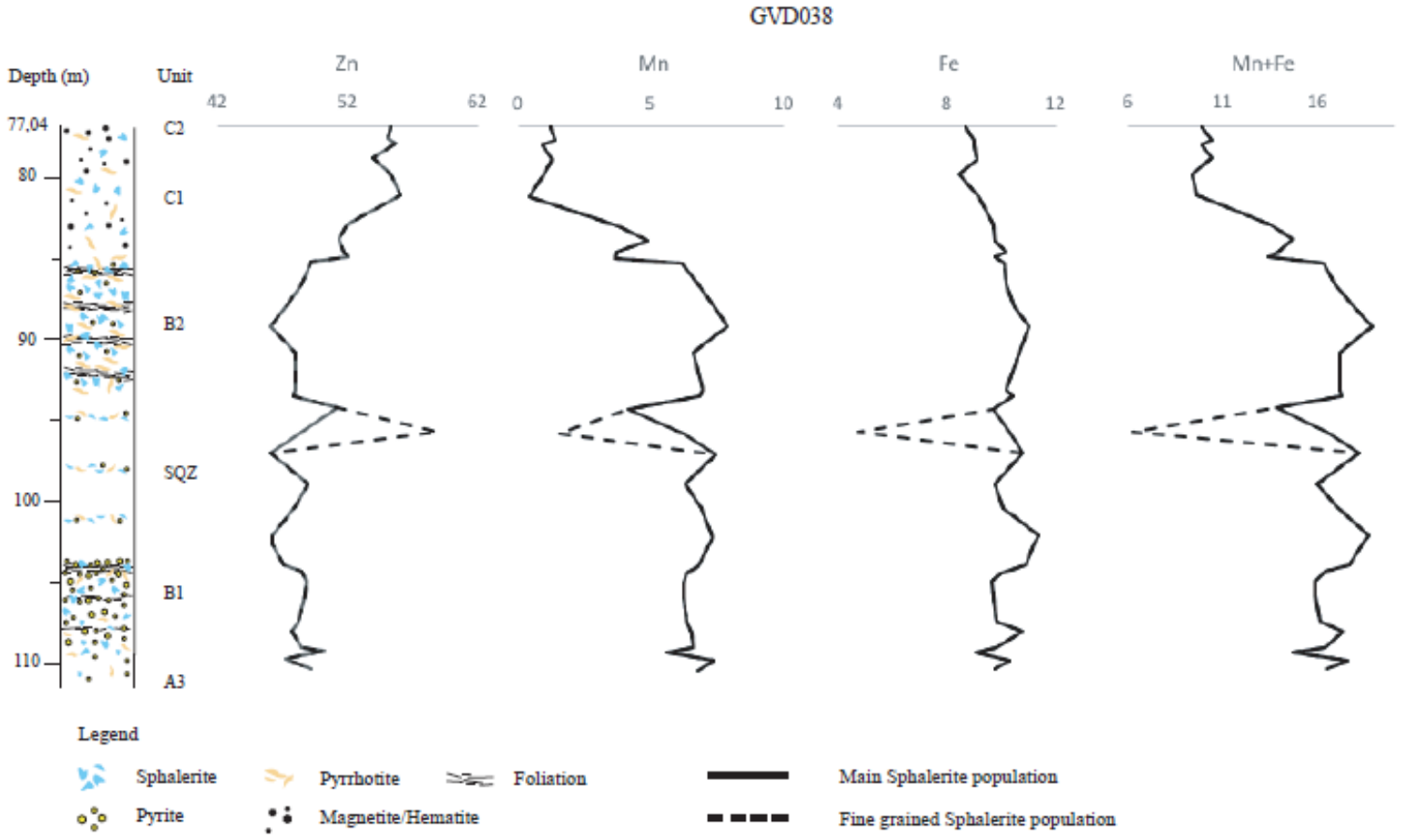

Figure 3: Sphalerite geochemical distribution profiles of Zn, Mn and Fe for drillhole GVD038 against its stratigraphy (from Poignant-Molina (2017)).

These geochemical profiles were also compared with sphalerite chemistry profiles from the North and East orebodies: the East orebody shows an analogous geochemical signal, whereas the North orebody presents a different geochemical pattern. *Poignant-Molina (2017)* interpreted these changes in the Zn, Mn and Fe concentration between the orebodies as the result of geomorphological and environmental variations within the primary basin in which the Gams Formation developed. Namely that the chemocline of the basin is defined by deep, more Mn-rich reduced waters and Mn-poor shallow waters, which is coupled with the basin topography that is higher in the northern part of the basin than in the southern part.

This study aims to obtain a further understanding of the genetic controls on the manganese content in the ore. The same 34 samples from the GVD038 drill core will be analyzed, focusing on variability of the stable sulfur isotope ratio throughout the stratigraphy and between the various sulfide minerals. Sulfur isotope fractionation is a redox sensitive process, not unlike manganese deposition, and this detailed study on the sulfur isotope variability will add a new dimension, redox, to our understanding of Gamsberg zinc deposit.

The goal of this study is to integrate new isotope data with the existing data on Fe/Mn variability to test the hypothesis from *Poignant-Molina (2017)* that the manganese enrichment in the ore is a result of primary genetic factors, and to produce a new genetic reconstruction of the orebody. This will be done by looking at the isotopic signature of the sulfide minerals throughout the stratigraphy and the differences in the isotopic signature between Mn-bearing and non Mn-bearing minerals.

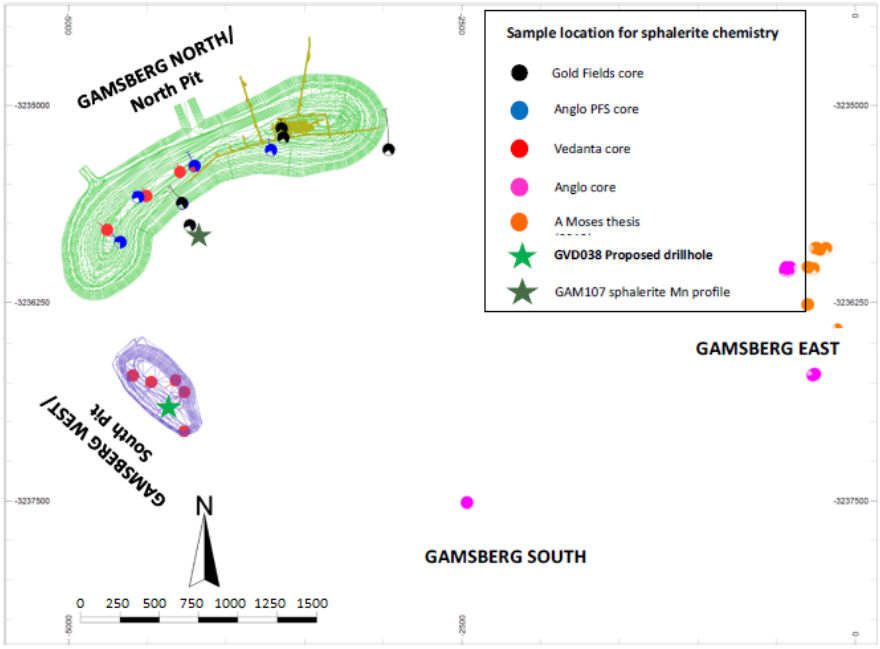

Figure 4: Locations of the two studied drillholes, GAM107 and GVD038, with other drillholes positions which their samples have been analyzed for sphalerite chemistry. The green and purple areas show the contours of the West and North orebodies (from Poignant-Molina (2017)).

1.3 Methodology

Stable S isotopes, represented by the ratio $^{34}S/^{32}S$, are useful for constraining environmental conditions and can be used to better understand the genetics of these ore deposits. Furthermore Mn-minerals are very sensitive to redox conditions, with alabandite (MnS) only being stable at a narrow range of redox conditions. Previous studies have shown that in the Aggeneys-Gamsberg deposits $\delta^{34}S$ values change from Pb- to Zn-rich ores, increasing towards the Zn-rich ores (*von Gehlen, 1983; McClung et al., 2011; McClung et al., 2007; Foulkes, 2014*). To see whether the isotopic S variation correlates with the stratigraphic patterns in the Fe/Mn ratio of sphalerite and vice-versa S isotope ratios first have to be quantified. In order to quantify the isotopic fractionation, the measured S isotope composition has to be correlated against a reference sample with known isotope ratios. The results relative to the reference material are reported in the "delta-notation":

$$\delta^{34}S_{ref} = (\frac{^{34}S}{^{32}S})_{sample}/(\frac{^{34}S}{^{32}S})_{ref} - 1) \times 1000$$

Sulfur isotopes are mainly fractionated during sulfate reduction (*Habicht and Canfield, 1997; Thode, 1991; Rees, 1973;*) which requires anoxia. Mn deposition can occur during Mn oxide production as well as the incorporation of Mn^{2+} into carbonate, but can also be incorporated in the mineral structure of sphalerite by substitution of Zn^{2+} with Mn^{2+} (*Deer et al., 1962; Cook et al., 2009; Ye et al.,*

2011). Mn oxide formation requires free oxygen and should therefore be more readily coupled to sulfide oxidation, a process that does not lead to extensive sulfur fractionation, rather than sulfate reduction. Thus while both processes involve redox, the chemistry involved is quite different. Therefore the expected result of this study is that when the Fe/Mn ratio's and δ^{34}S values are both superimposed on the stratigraphy, these chemical signals will not show the same behavior. If these chemical signals reveal an inverse relationship throughout the stratigraphy, this would be a strong indication that redox is the main controlling factor on the manganese content in the Gamsberg deposit.

1.3.1 Analysis

First the petrography of the samples was mapped in order to efficiently find the mineral grains that are most suitable for chemical analysis (i.e. large enough that the mineral surface comfortably encompasses the 120μm spot size of the excimer laser and homogeneous in the sense that there are no, or as few as possible, inclusions present in the spot that will be analyzed). Prior to mapping the samples, the samples were repolished in order to remove any carbon coating that may have remained from previous SEM analyses on this set of samples (*Poignant-Molina, 2017*). The samples were mapped by optical microscopy using reflected light. The microscopic observation was carried out using the Leica DMRX light optical polarization microscope of the High Pressure and Temperature Laboratory of the department of Geosciences at Utrecht University. The photographs were taken using the Leica Application Suite (LAS). The photographs were stitched together to create overview images of the samples using the stitching plug-in of the FIJI distribution of image analysis software ImageJ (*Schneider et al., 2012; Schindelin et al., 2012*).

Analyses using Laser Ablation Inductively Coupled Plasma Mass Spectrometry (LA-ICP-MS) were performed on the Sphalerite, Pyrite, Pyrrhotite and some minor sulfide phases to produce the core data set for this study. Quantitative chemical analyses of these sulfides were obtained using the ThermoFischer Scientific Element 2 magnetic sector ICP-MS of the GML lab at Utrecht University, equipped with a Geolas (MicroLas, Goettingen, Germany) 193 nm excimer laser ablation system. *Table 1* shows the parameters using which the analyses were performed. Counts were recorded for both ^{32}S and ^{34}S. The recorded isotope data was then calculated relative to S isotope reference material MASS-1 (also known as PS-1), which has a known value of δ^{34}S = +5.85‰ compared to the internationally recognized standard Vienna Canyon Diablo Troilite (VCDT) with δ^{34}S = 0.0‰ by definition (*Fu et al., 2016; Krouse & Coplen, 1997*).

2 Background on ore forming processes

2.1 SEDEX deposits

Sedimentary exhalative (SEDEX) deposits are laminated or bedded, sulfide rich tabular bodies hosted by pyrite bearing or carbonaceous, fine grained, clastic rocks; and account for more than 50 percent of the world's zinc and lead reserves (*Tikkanen, 1986*). The primary diagnostic feature of these deposits in the field

is the laminated bedding-parallel texture of the sulfide ore minerals. These deposits generally contain a series of ore lenses stacked within barren pyritic and carbonaceous siltstones and shales (*Large et al., 2002*). These deposits represent chemical sediments that are precipitated from hydrothermal fluids, which are derived from vents, onto the sea floor. These general criteria used to define a deposit type, however, are subject to debate (e.g. *Eldridge et al., 1993; Leach et al., 2005*), which leads to some authors to use more descriptive names for these deposits such as sediment-hosted stratiform Zn-Pb-Ag deposits, rather than SEDEX (*Large et al., 2002; Emsbo, 2009*).

The process of SEDEX deposit formation is driven by base metal bearing hydrothermal fluids, which are, based on isotopic research, most likely derived from the underlying sediments from the host basin. These hydrothermal fluids flow through the sedimentary basin towards the sea floor where mineralization and subsequent precipitation of the metal ore occurs (*Emsbo, 2010*). SEDEX deposits can be found in extensional fault-bound first order intracratonic and epicontinental basins with dimensions exceeding 100km. Within these large basins smaller second-order basins can be present in the form of half-graben structures which generally occur on a scale of tens of kilometers. The extensional faults in these second-order structures act as a interconnected fluid pathways which allow hydrothermal brines from the deeper strata to find their way to the sea floor (*Emsbo, 2009; Leach et al., 2005*). On an even smaller scale, within the second-order basins, third-order basins on the scale of only a few km can be found. These small basins enable euxinic conditions to develop, are characterized by low energy and are dominated by pyritic fine-grained shales and mudstones that have a relatively high organic content. The low bathymetry of these third-order basins along with their euxinic chemistry provides the ideal environment for the dense, base metal-bearing brines to accumulate and react with H_2S to form the various sulfide minerals that make up the SEDEX ore (*Emsbo, 2009; Large et al., 2002*).

Fluid inclusions in the SEDEX deposits have shown that the hydrothermal fluids from which SEDEX ores are derived have a temperature from 100°C to 300°C and a salinity between 10-30 wt-% of total dissolved solids (TDS) (*Gardener and Hutcheon, 1985; Leach et al., 2004; Emsbo, 2009; Large et al.,2002*). When these hot hydrothermal brines come in contact with the cold, euxinic seawater the solubility of the metals in the brine decreases sufficiently to have them precipitate from solution and allow for reactions with H_2S to happen. Analysis of modern brines alongside chemical modeling has demonstrated that the most important controls on the high solubilities of Zn and Pb in +100°C brines are high salinity and a low H_2S concentration. Even moderate amounts of H_2S drastically decrease the solubility of these metals in the brine. The solubility of some base metals in SEDEX brines is extremely low when sulfate is present (eg. Barium which will readily precipitate with the sulfate to form barite) (*Kharaka et al., 1987; Emsbo, 2009*).

The dominant control of the H_2S concentration on metal solubility makes it a very important parameter in basin processes. In sedimentary basins H_2S is generated by thermochemical sulfate reduction (TSR), the thermal decomposition of organic carbon such as kerogen, coal and high-sulfur oils (*Hunt, 1996; Emsbo, 2009*). The temperatures required to get geological significant rates of

TSR can be reached when at least 3 km (or more in exceedingly deep basins) of sediment fill exists above the crystalline basement of the sedimentary basin (*Emsbo, 2009*). H_2S may also be produced in the top sedimentary layer at the water-sediment interface by sulfate reducing microbes. Removal of H_2S in hydrothermal brines is primarily controlled by the concentration of Fe, which reacts with the H_2S to form pyrite (FeS_2). In order to have a brine that has the capability to chemically buffer H_2S, allowing the other base metals to remain in solution; oxidized rift-fill continental rocks (e.g. red beds) in association with fluvial-deltaic and shallow marine continental clastic sequences form the ideal Fe-rich, organic carbon-poor source material (*Hunt, 1996; Emsbo, 2009*).

The base metal content in these brines is derived from various source sediments in the host basins. The sources of these components can be derived in more detail by studying the radiogenic and stable isotope compositions of the ore components. Previous studies have demonstrated that continentally derived clastic sediments in the host basin are the source of Pb and Sr (*Ayuso et al., 2004; Emsbo And Johnson, 2004; Large et al., 2005; Leach et al. 2005*). Moreover, other base metals are likely derived from coarse grained, oxidized clastic sediments (eg. Conglomerates, red beds, sandstones) in underlying rift-fill sequences (*Emsbo, 2009*).

The most abundant element by mass in SEDEX deposits, however, is Sulfur. The sulfur in SEDEX deposits has a marine origin, and is later reduced from sulfate to sulfide by microbial or thermogenic reduction. *Emsbo (2009)*, argued that lacustrine water is an unlikely source of sulfate as sulfate levels are generally two orders of magnitude lower in lacustrine environments and is thus unlikely to harbor the amount of sulfate necessary to sequester the amount of metal found in major SEDEX deposits. A further indication that the presence of reduced sulfur derived from marine sulfate is linked to the formation of SEDEX deposits may be the absence of Archean SEDEX deposits, as the Archean was characterized by low-sulfate oceans (*Lyons et al., 2006; Goodfellow, 2007*).

2.2 Broken Hill-Type (BHT)

Broken Hill-type deposits are a sub-classification of SEDEX deposits that have some distinctive chemical features (Figure 5):

- BHT deposits commonly show higher Pb/Zn ratio's and higher Ag content compared to general SEDEX deposits (*Leach et al., 2005; Large et al., 2002*).
- Some of these deposits contain stratiform Pb-rich lenses which are poor in zinc, which is uncommon in SEDEX deposits (*Large et al., 2002*).
- BHT deposits generally have a different chemical signature than SEDEX deposits: SEDEX deposits are generally enriched in Mg, Ca, Fe, Ba, Mn and Tl; whereas BHT deposits show a Ca, Fe, Mn, P, F, Si and REE enriched chemistry. Although Ca, Fe and Mn are enriched in both deposit types, it has to be noted that Mn enrichment in BHT is significantly

greater than in SEDEX due to the BHT deposits occurrence in more oxidized sedimentary environments (*Large et al., 2002*).

- BHT deposits contain magnetite, a mineral not associated with SEDEX ore systems.

Besides distinct chemical differences, the geologic setting and associated lithologies also allow for clear differentiation between the two types of deposits:

- All BHT deposits are found in high-grade metamorphic sedimentary terrains, however it is debated if post-formational metamorphism of a deposit should be a used as a criterion to distinguish between deposit types (*Emsbo et al., 2016*).
- The associated lithologies in the regional geological sequence varies from quartzo-feldspathic to pelitic dominated. This reflects a component of footwall felsic volcanics and arkosic clastic material that is greater than normally found in SEDEX sequences (*Large et al., 2002*).
- The immediate host rocks to the BHT deposits also differ significantly from those of SEDEX deposits. SEDEX host rocks are of carbon-rich, organic shale- or siltstone facies. BHT host rocks on the other hand may include sulfide, silicate, oxide and carbonate facies. This mixed package shows variable redox conditions in the depositional basin, from highly oxidized (e.g. BIF and manganiferous exhalite) to highly reduced (e.g. graphitic sulfide ores) (*Large et al., 2002*).

Despite the numerous differences between BHT and SEDEX deposits making them readily distinguishable from each other (Figure 5), one of these distinguishing features, namely the high-grade metamorphism of the BHT deposits, greatly complicates constraining the genetic processes of these deposits, leading to many conflicting hypotheses on the genesis of BHT deposits (*Parr and Plimer, 1995; Davidson, 1996; Large et al., 2002*).

The Gamsberg deposit displays characteristics of both SEDEX and BHT deposits. BHT characteristics include metamorphic terrain, pyrrhotite-rich ore units and high Zn concentrations. SEDEX is represented by the presence of pyrite-rich ore units and graphitic-rich metapelites, as well as an association with barite and a wide range of δ^{34}S values in the ore (6.2-32 per mil [‰]). Thus, the Gamsberg deposit can be defined as an intermediate deposit (*Leach et al., 2005, Spry et al., 2009; Emsbo et al., 2016*).

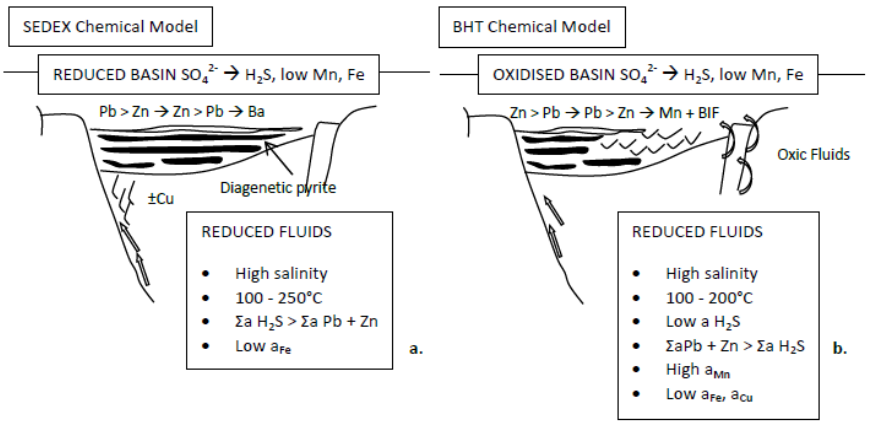

Figure 5: Chemical models for (a) SEDEX genesis; and (b) BHT genesis. (From Foulkes (2014): After Large et al., 1996.)

3 Geological background

3.1 Regional setting

The Aggeneys-Gamsberg mining district is located in the Namaqua Sector in the north-eastern region of the Namaqua-Natal Province in South Africa (Figure 6). The Namaqua-Natal Province or Namaqua-Natal Mobile Belt is an aggre-

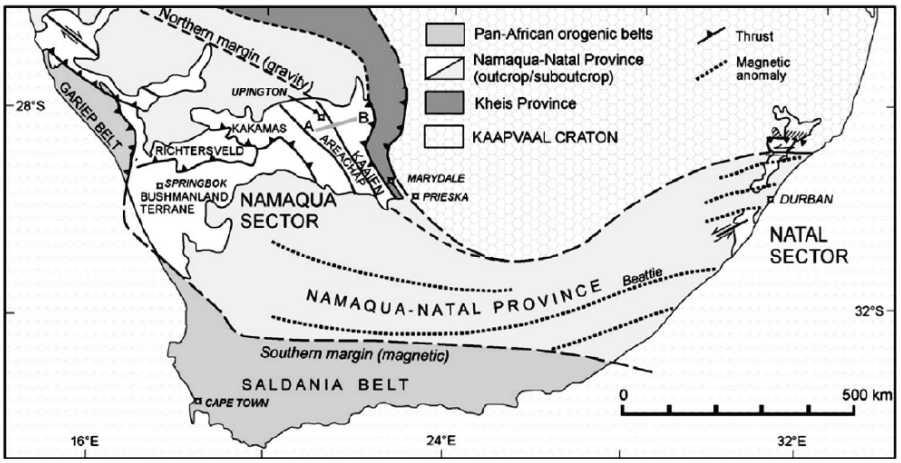

Figure 6: Schematic diagram of the geological setting of the Namaqua-Natal Province (from Cornell et al. (2006)).

gation of medium to high-grade metamorphic terranes that is ± 400km wide and stretches from southern Namibia southeastwards to the Northern Cape Province in South Africa to Kwazulu-Natal on South Africa's eastern seaboard. The Namaqua-Natal province is bound by shear zones, is compressed against

the southwestern and southern margins of the Archean Kaapvaal Craton and is part of a Mesoproterozoic orogenic belt that also includes the Namibian Namaqua Metamorphic Complex, the Ngamiland belt in Botswana and the Zambian Choma-Kalomo Block (Figure 7) (*McCourt et al., 2006; Cornell et al., 2009;*). The Namaqua-Natal Province formed during the construction of the Rodinian supercontinent (*Thomas et al., 1994; McCourt et al., 2006; Bailie et al., 2007a*). The Namaqua Sector or Namaqua Metamorphic Complex on the western side of the province hosts a succession that can be subdivided into 5 metamorphic terranes which are characterized by medium- to high-grade metamorphosed volcano-sedimentary supracrustal sequences (±2.0 Ga)(*Thomas et al., 1993*) that are intruded by granitoids (1.2-1.0 Ga)(*Thomas et al., 1993*). These terranes include: The Areachab Terrane, the Kakamas Terrane, the Bushmanland Terrane, the Kaaien Terrane and the Richtersveld Terrane. Several deformational events were recorded in this terrane succession (*Thomas et al., 1994*).

The morphology of the region was shaped by two major tectonic events between 1.21 and 1.03 Ga. The Kibaran orogeny (1.21-1.17 Ga)(*Robb et al., 1999*) is the result of the collision of the Namaqua-Natal Belt with the Kaapvaal Craton and resulted in crustal thickening of the region. The Namaquan (1.06-1.03 Ga)(*Robb et al., 1999*) orogeny is a more discrete heating event that caused thermal reworking of the proliths in the region. The metamorphic overprint in Namaqualand and the granitoid intrusions in the metamorphic terranes can be ascribed to these two events (*Robb et al., 1999; Thomas et al., 1994; Bailie et al., 2007b; Dewey et al., 2006*).

3.2 The Bushmanland Terrane

The area of interest in this study, the Aggeneys-Gamsberg mining district is located within the Bushmanland Terrane. The surface morphology of the Bushmanland Terrane is characterized by isolated mountains (inselbergs) amidst otherwise flat plains. The lithostratigraphy of the Bushmanland Terrane is by some authors (e.g. *Cornell et al., 2006*) divided in three main lithologies: The granite dominated Kheisian gneiss basement, supracrustal volcano-sedimentary sequences which overlay this basement and dispersed intrusions. Other authors such as *Bailie et al., (2007a)* argue that the supracrustal sequences show too much variation between the different inselbergs to define a "one sequence fits all" for the whole Bushmanland Terrane and proposed several stratigraphic interpretations for the Bushmanland Terrane. For the sake of convention and to avoid unnecessary confusion, the same stratigraphy as was chosen by *Poignant-Molina (2017)* will be chosen for this study. This stratigraphy is the adaptation of the works of *Stalder and Rozendaal (2004, 2005)* by *Moses (2015)* (Figure 9), which corresponds well in the Aggeneys-Gamsberg area and focusses on the Gamsberg Zn deposit.

3.2.1 The granitic basement

The granitic basement in the Aggeneys-Gamsberg area was divided by *Bailie et al. (2007b)* into three distinct granitic gneisses with characterizing petrographic

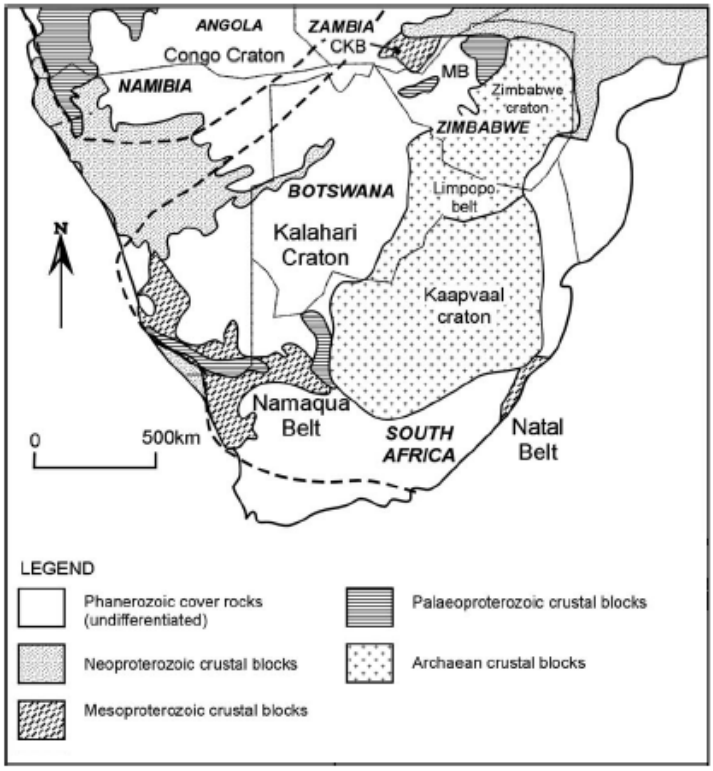

Figure 7: Schematic diagram of the geological framework of southern Africa. MB = the Paleoproterozoic Magondi belt in Zimbabwe; CKB = the Mesoproterozoic Choma-Kalomo block in Zambia (modified from McCourt et al. (2006)).

features: the Achab Gneiss, the Aroams Gneiss and the Hoogoor Gneiss. The spatial distribution of these rocks is shown in Figure 8.

The Achab Gneiss surfaces predominantly in the eastern part of the district (Figure 8). This unit hosts coarse microcline and microperthite porphyroblasts inside a fine- to medium grained matrix of biotite, quartz and plagioclase. Parts of the Achab Gneiss in high strain areas are banded. Although the Achab Gneiss has been interpreted by various authors as a metamorphosed arkose, pre-Bushmanland Group basement or an intrusion into the supracrustal succession, relatively narrow ranges of SiO_2/Al_2O_3 ratios have been found that more closely resemble igneous rocks than a suite of sediments (*Bailie et al., 2007b; Reid et al., 1997*).

The Aroams Gneiss is the most dominant gneiss suite in the Aggeneys District, is located predominantly in the northeast of the district and consists of a series of gray megacrystic gneisses with augen textures composed of microcline and quartz. The Aroams Gneiss displays intrusive features and is therefore correlated to the 1.2-1.18 Little Namaqualand Granitoid Suite (*Figure 8;Stadler and Rozendaal, 2005a; Reid et al., 1997; Bailie et al., 2007b*).

The Hoogoor Gneiss, sometimes called "Pink Gneiss" or "Haramoep Gneiss" due to its characteristic pink color, is a series of quartzofeldspatic gneisses that occurs throughout the Bushmanland Subprovince (Figure 9). This unit is strati-

graphically located between the other gneiss units and the Bushmanland group. The Hoogoor Gneiss is void of megacrysts and augen textures and is moderately well foliated. The Hoogoor Gneiss is often included into the Bushmanland group due to its physical distinctions with the Achab and Aroams gneisses, the close proximity to the supracrustal sequences and the presence of discontinuous schist layers from the overlaying unit (*Bailie et al., 2007b; Reid et al., 1997*).

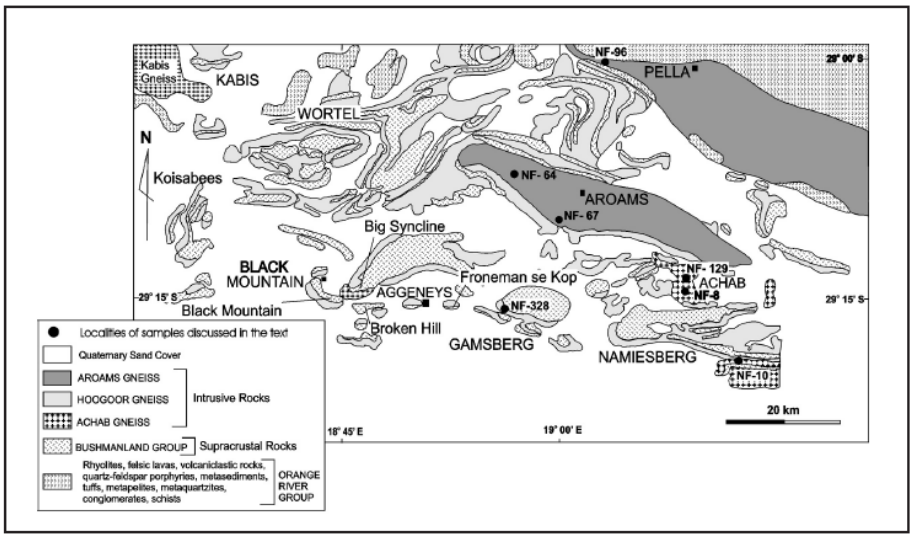

Figure 8: A locality map of the Aggeneys-Gamsberg district showing the spatial distribution of the various granitic gneiss units. Note that the black dots are not relevant for this study (from Bailie et al. (2007b)).

3.2.2 The Bushmanland Group supracrustal sequences

The Bushmanland group is divided in two formations: the Wortel Formation and Kouboom Formation which overlays the Wortel Formation. These formations are both subdivided in two units (Figure 9). At the bottom of the stratigraphy of the Wortel formation lays the Namies Schist which sits on the granitic gneiss basement. This 80m thick unit is an aluminum-rich metapelitic schist with quartz, K-feldspar, muscovite, biotite and sillimanite making up the dominant mineral assemblage (*Stalder and Rozendaal, 2005*).

The Pella Quartzite contains a dark recrystallized quartzite unit and a white recrystallized quartzite unit that are interbedded by pelitic schists (*Bailie et al., 2007a*). The Pella Quartzite forms the top unit of the Wortel Formation which is interpreted as a metamorphosed sequence of shallow-water quartz arenites and black shale containing mudstones (*Stalder and Rozendaal, 2005*).

The Gams Formation, my formation of interest and sometimes called the Aggenyes Ore Formation, is a Zn-Pb-Cu-Ag-bearing ore body that consists of metapelitic schist with a complex mineralogy that is interbedded with quartzite, iron formations, barite beds and calc-silicate rocks (*Stalder and Rozendaal, 2005a; Ryan et al. 1986*). The Gams Formation marks the bottom of the Kouboom Formation and overlays the Wortel Formation with a sharp contact. The 200m thick

Gams Formation can be subdivided into three members: A, B and C (*Rozendaal 1975; Stalder and Rozendaal, 2002*), which will be described in more detail in the next section.

The top unit of the Bushmanland Group's Kouboom Formation is the Nousees Mafic Gneiss (*Rozendaal, 1975*) or Koeris Gneiss (*McClung et al., 2002*) which is seperated from the Gams Formation by an unconformity. The Koeris/Nousees Gneiss is a succession of conglomerate, metapelitic to metapsammtic schist, amphibolite and quartz-feldspar-muscovite gneiss (*Stalder and Rozendaal, 2005; McClung et al., 2007*). The youngest depositional unit of this member, an amphibolite, has been dated at ±1649 Ma (*Stalder and Rozendaal 2005*).

The absolute age envelope of the Bushmanland Group, however, is unsolved although some constraints are made by previous authors. *Bailie et al., (2007b* present a 2.05Ga age for the Achab Gneiss, the basement to the Bushmanland Group. The deposition of the Bushmanland Group, including the Gams Formation is placed at 2.0-1.8Ga by these authors. *Cornell et al., (2009)*, however, argue that the Bushmanland Group was deposited around or before 1.6Ga. Amphibolites in the overlying Koeris Formation have been dated at 1.65±0.09Ga by *Reid et al., (1987).*

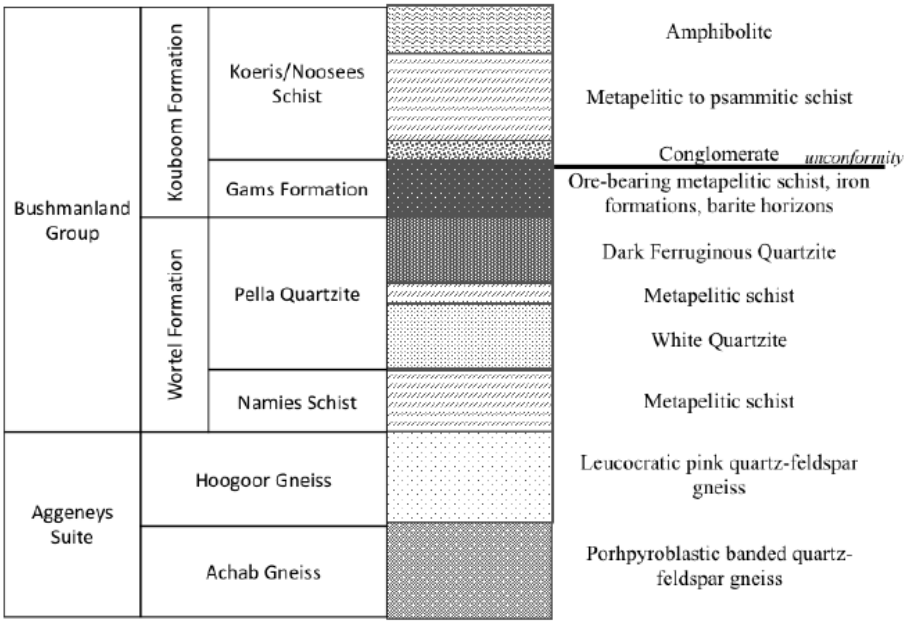

Figure 9: Simplified stratigraphy of the Aggeneys-Gamsberg district (from Moses (2015) after Stalder and Rozendaal (2005)).

3.2.3 Structure and Metamorphism

The Bushmanland Terrane and by extension the Aggeneys-Gamsberg ore district are metamorphosed and structurally complex terrains due to polyphase deformation events which can be attributed to the Kibaran and Namaquan orogenies (*Robb et al., 1999*). The most widely accepted structural analysis of the

Bushmandland Terrane is that of *Joubert (1971)*, which carefully detailed the different deformation and metamorphism phases. These deformational phases (D1-D5) were summarized by *Bailie et al. (2007a & 2007b)*:

- **D_1:** The first deformation phase is represented by tight isoclinal (F_1) folds that have been overprinted by subsequent deformation.
- **D_2:** This second deformational phase, which is the most important deformation phase, was accompanied by the peak of upper amphibolite grade metamorphism (M_2). Under upper amphibolite grade metamorphic conditions pyrite can break down and form pyrrhotite (*Craig and Vokes, 1993*). This deformation phase is represented by recumbent isoclinal folds (F_2) that plunge towards the northeast. Thrusting associated with this deformation phase is dominant in the structural pattern of the gneisses and resulted in structural duplication.
- **D_3:** The third deformational phase was accompanied by the third metamorphic phase (M_3) and is represented by large scale, asymmetric, open folds east-north-east striking folds(F_3).
- **D_4:** This phase resulted in northward-trending monoclinal folds and northerly and northwesterly oriented faults.
- **D_5:** The final deformation phase is characterized by north-east trending strike-slip faults and shear zones.

The metamorphic history of the Namaqualand Metamorphic Complex is most pronounced by the M_2 phase, a high T/low P event that produced metamophic grades going up to the upper amphibolite to granulite facies, followed by the M_3 phase which had a retrograde pathway and produced overprinted greenschist and amphibolite facies (*Willner, 1995*). Peak metamorphism continued for some time after the main deformational event (D_2) but ceased before the third deformation event, D_3 (*Willner, 1995*). Using the mineral assemblages in the Bushmanland Terrane as a geothermobarometer, *Cornell et al. (2006)* place the upper amphibolite facies in the north, containing biotite, sillimanite and quartz, at a temperature of 650-700°C with a pressure of 4 kbar. The southern granulite facies which contains cordierite, garnet, K-feldspar, quartz and hercynite is placed at PT conditions of 830°C and 5-7 kbar.

The Aggeneys-Gamsberg district underwent a clockwise PTt path that is associated with amphibolite facies through the D_2 deformation episode (*Stalder and Rozendaal, 2004; McClung et al., 2007; Bailie et al., 2007b, Willner 1995*). The prograde PT conditions at Gamsberg were constrained at 630-670°C and 2.8-4.5 kbar and fall in the upper amphibolite facies, based on the mineral assemblage (cordierite, sillimanite, K-feldspar, quartz and muscovite) (*Rozendaal, 1975; Rozendaal, 1984; Hoffmann, 1994;*). The retrograde PT conditions were determined using sorosilicates and chlorites and found to be cooler at 550-600°C (*Rozendaal, 1975; Willner, 1995*).

3.3 Geology of the Gamsberg Deposit

The Gamsberg Zn deposit is confined to a stratiform ore horizon, the Gams Formation, inside a steep-sided inselberg of 7 by 5 km. This inselberg, the Gams-

berg, is the surface expression of a single mega-sheath-fold which morphology was constructed by three phases of deformation (Figure 10) (*Stalder and Rozendaal, 2004; Moses, 2015*). These three subsequent deformation phases (F_1,F_2 and F_3) were able to shape the complex circular morphology of the Gamsberg whilst preserving the structural integrity of the orebody due to the plasticity of the metasedimentary units. F_1 is represented by a north-south oriented synformal folding which occured conjointly with east-west oriented synformal folding associated with F_2 to produce large-scale sheet folding of the basin. F_3 is a later north-east oriented vertical synformal folding event that is superimposed on the pre-existing structures (*Stalder and Rozendaal, 2004*).

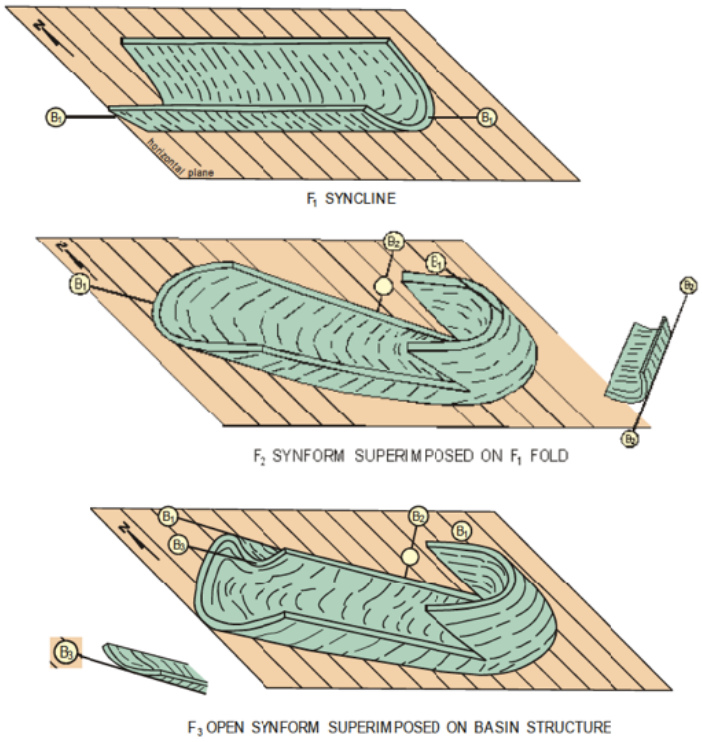

Figure 10: Schematic overview of the various deformation phases responsible for the morphology of the Gamsberg Zn deposit (F_1,F_2 and F_3) (from Poignant-Molina (2017) after Moses (2015)).

3.4 Petrography and lithostratigraphy of the Gamsberg deposit

The Gamsberg deposit is divided into four main ore bodies: North, East, South and West (Figure 11). The stratigraphy of the Gamsberg deposit (Figure 12) bears similarities to the regional stratigraphy of the Bushmanland overlaying the Hoogoor basement (Figure 9). One of the main orebodies, East, however is stratigraphically inverted compared to the other ore bodies due to deformation that is also associated with the genesis of the "overturned limb".

The Gams Formation is divided into three members (from old to young: A, B and C). Member A has a thickness ranging from 10 to 30m and consists of a thin basal garnet-pyroxene-amphibole-magnetite rock (A2), which is overlain by impure marbles (A3). The top of member A is marked by a unit of fine-grained banded quartz-garnet-feldspar-clinopyroxene rocks (A4) (*Stalder and Rozendaal, 2004*).

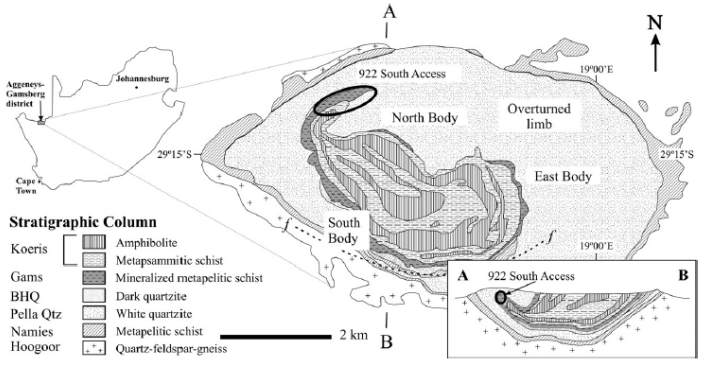

Figure 11: A geological map of the Gamsberg deposit. BHQ = Broken Hill Quartzite; Qtz = Quartzite. Note: The circle outlining the "South Access" at the North Body is not relevant for this study. (From McClung and Viljoen (2011) after Stalder and Rozendaal (2004) and McClung (2006)).

Member B has a thickness of 25 to 50m and represents the mineralized sulfide zone which is the unit of interest for this study and where the bulk of the samples is derived from (Figure 13). The basal unit (B1) contains less mineralized, metapelite-hosted ores. This unit contains graphite-rich quartz-sillimanite-muscovite ±feldspar schists, which *Rozendaal (1986)* interpreted to represent the original organic-rich mudstones. This unit is rich in pyrite (up to 30wt%) in association with varying amounts of sphalerite. The overlaying B2 unit consists of high-grade calc-silicate-hosted ores in the form of mineralized and well-banded quartz-garnet-amphibole rocks which indicate chemogenic origin (*Stalder and Rozendaal, 2004*). A peculiar part within the B1 unit is a sulfidic quartzite that is intercalated in the this unit in the West Body, this part is included in the samples used in this study(*Poignant-Molina, 2017*).

At the bottom of the B2 unit a 3-m-thick laterally continuous phosphatic layer that contains abundant nodular apatite in a quartz-muscovite-sillimanite matrix. This Apatite Marker unit (AMU) stands out as a sharp boundary where the dominant Fe-sulfide changes from pyrite (B1) to pyrrhotite, which suggest this unique layer marks some paleo-redox boundary (*Stalder and Rozendaal, 2004*).
The C member that overlays the ore horizon is mostly devoid of iron- and base metal sulfides, but is rich in Fe-oxides and Fe-Mn silicates. The bottom unit of this member, C1, contains a variety of Fe-Mn-rich rocks types and shows a transition from the North Body to the Overturned Limb with silicate- and carbonate-rich meta-exhalites grading into oxidized iron formations (magnetite and/or hematite). The topmost unit of the Gams Formation in the C2 unit which is composed of various laminated andradite-calderite-rich rocks and hosts

variable concentrations of rhodonite and Fe-Mn amphibole (*Stalder and Rozendaal, 2004*).

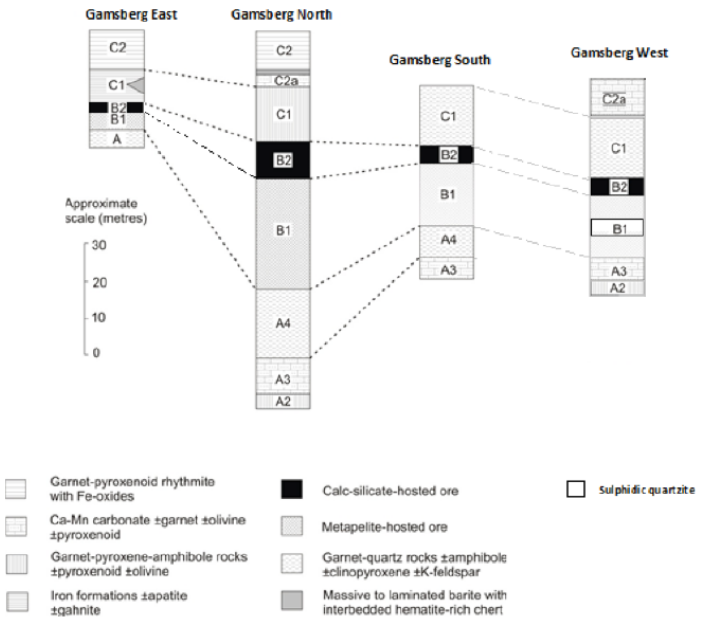

Figure 12: Lithostratigraphic columns for the different Gams Formation constructed for the different orebodies, showing the variations and correlations in the Gams Formation between the various orebodies (from an unpublished report by Vedanta (2017)).

3.5 Drillhole GVD038

A detailed microscopic petrographic description of the sulfide rich zones encountered in drillhole GVD038 was done by *Poignant-Molina (2017)*, who analyzed the exact same sample set that is used in this study. Therefore the petrography of the samples from top to bottom throughout the stratigraphy will be summarized here based on the extensive description produced by *Poignant-Molina (2017)*.

This study uses the same nomenclature for the stratigraphy as the relevant literature. However, as this study and the study of *Poignant-Molina (2017)* both aim as a secondary objective to draw comparisons to the geochemical analysis carried out by Vedanta Resource Limited on drillhole GAM107, which uses a different nomenclature, both nomenclatures are listed in the table in Figure 13 to avoid confusion when comparing this study with that of Vedenta (*unpublished study, cited by Poignant-Molina, 2017*).

3.5.1 Mineralogy and Textures: C2 unit

The mineralogical assemblage of C2 is dominated by a massive equigranular package of iron oxides, sulfides and gangue minerals including garnet, quartz, amphibole and pyroxenoid. The defining texture is granoblastic with minerals sizing from 0.5 to 3mm. Amphibole was reported in the C2 unit (*Vedanta,*

Lithology Vedenta	Nomenclature Vedanta	Literature	Samples
Garnet-Amphibole-Magnetite	GAM	C2	18A, 18B
Garnet-Magnetite Ore	MPO	C1	20A, 20B, 21A, 22A, 24A, 25A, 25B
Pyrrhotite Ore	PEO(Po)	B2	26A, 26B, 26C, 27A, 29A, 29B, 31A, 31B
Sulfidic Quartzite	SQZ	SQZ	33A, 34A, 34B, 35A, 36A, 37A, 38A
Pyrite Ore	PEO(Py)	B1	40A, 40B, 40C, 41A, 42A, 42B
Meta-pelite	PEL	B1	43A, 44A, 44B, 44C
Calc-silicate	CAS	A3	-

Figure 13: Comparison of nomenclature used in the drillhole GVD038 for the Gams Formation and list of samples by unit (from Poignant-Molina (2017)).

2017) but not encountered in these samples. Furthermore clinopyroxene, K-feldspar, chlorite, zoisite and calcite were reported in the C2 unit in minor to major amounts (*Rozendaal, 1986*) but not encountered as well.

SEM analysis of the gangue minerals by *Poignant-Molina (2017)* showed a high Mn content in garnet and pyroxenoid minerals, indicating that these are present in the form of spessartine or calderite and rhodonite respectively.

Sulfide minerals in this unit are dominated by pyrrhotite and sphalerite, as well as a minor presence of pyrite. The more ductile sulfides, sphalerite and pyrrhotite, are severely affected by deformation causing them to plastically migrate in grain boundaries and micro fractures between the more robust grains. Pyrite is found in fine- to medium-grained inclusions in the coarser pyrrhotite. Iron oxides are present as hematite and magnetite with ilmenite as an accessory mineral phase. The dominant Fe-oxide in the C2 unit is hematite, but is gradationally replaced by magnetite towards the bottom of the unit.

3.5.2 Mineralogy and Textures: C1 unit

The C1 unit underlays the C2 unit and has a similar mineralogical composition. The general granoblastic texture containing quartz, garnet, Fe-oxides and sulfides is continued. The gangue minerals present the same overall morphologies. The difference between the C1 and C2 units comes from the gradational transition between the B and C members. This is marked by an increase of sulfide minerals at the cost of iron oxides and gangue minerals. Furthermore there is an increase in base metals in C1 compared to C2 with localized development of galena and a higher modal distribution of sphalerite in the C1 unit. Fine grained apatite nodules were observed as well, indicating the presence of phosphorus in the Gamsberg deposit.

Pyrite can be found as idiomorphic or sub-idiomorphic crystals, often associated with pyrrhotite.

3.5.3 Mineralogy and Textures: B2 unit

The B member contains the bulk of the base metal mineralization in the Gams Formation, with the B2 unit containing the higher ore grades. The mineralization is mainly composed of fine- to medium-grained anhedral sphalerite and pyrrhotite with minor sub-euhedral to euhedral pyrite. Galena and chalcopyrite are found in smaller amounts as well. The gangue minerals are again dominated by quartz and garnet. Apatite, K-feldspar, zircon, zoisite and clinozoisite appear as fine-grained accessory minerals. The B2 unit also contains a higher concentration of micas (biotite and muscovite) which display a foliation. In some places micro-folding is recorded by alteration, cleavage and/or inclusions in the sulfides which show complex patterns, that indicate a late deformational event that post-dated the ore mineralization.

In coarser pyrite aggregates exsolution of sphalerite can be observed in this unit. Inversely, annealed grain boundaries of pyrite grains included into anhedral sphalerite are recurrent this unit. Some of these display poikiloblastic pyrite grains, interpreted as features of when apparent resorption reached an advanced stage.

3.5.4 Mineralogy and Textures: SQZ unit

The sulfidic quartzite (SQZ) unit occurs in the West and South orebodies of the Gamsberg deposit and represents a 9 to 10m thick quartzite with intercalated, irregular sulfide-rich meso-bands. The sulfides are mainly fine- to coarse-grained sub-euhedral to xenomorphic pyrite, pyrrhotite and sphalerite. There are some sharp contacts between some sulfide-rich and sulfide-poor areas. The contacts between the sulfide-rich and sulfide-poor zones that are gradational, rather than sharp, are marked by disseminated fine grained sulfides in the quartz-dominated granoblastic rock. The core of the meso-bands consists of aggregates of coarse sulfides with sphalerite being the main phase. In these coarse crystals alteration is prevalent, with very fine- to medium-sized dark spots are recurrent. The exsolutions observed in the coarse sphalerite crystals are blebs of alabandite and galena, which may denote a geochemical reconstitution of the sulfide ore during metamorphism. Another secondary feature in this unit is the presence of pyrite overgrowths surrounding a sphalerite core, which is also interpreted as a metamorphic texture formed during re-equilibration during annealing. Manganese was also found in minor oxide phases, interpreted as pyrolusite (MnO_2).

3.5.5 Mineralogy and Textures: B1 unit

The B1 unit is less mineralized than the B2 and SQZ units. Pyrite has replaced pyrrhotite as the dominant Fe-sulfide phase and a substantial amount of graphite can be found in this unit. The upper part of this unit exhibits moderate banding attributed to mineralogical variations, specifically the association of silimanite, muscovite and sphalerite as elongated grains that show a preferred orientation and define an irregular wavy foliation. The bottom part of the unit, approaching the contact with the A member, shows an apparent reduction in the degree of foliation in favor of a more massive ore body. This feature continues until a fine-grained disseminated sulfide zone, called the "PEL unit" by Vedanta geologists, is reached.

Pyrite in this unit developed as aggregates of sub-euhedral, rounded grains in massive domains or as elongated anhedral grains in foliated zones. Some zones show brecciation that is produced by intense deformation that resulted in fracturing of the pyrite grains against each other and ductile sulfides such as sphalerite and pyrrhotite filling in these micro-fractures. 120° angles were observed at pyrite grain triple junctions, albeit less common than interstitial sulfide minerals filling micro-fractures. These are 120° angles are interpreted as recrystallization of pyrite in this unit as a result of thermal metamorphism.

The second most abundant in the B1 unit is sphalerite that is more anhedral in the disseminated sulfide zone compared to pyrite. Sphalerite occurs as apparent fibrous intergrowths with sillimanite or muscovite, or similarly to the SQZ unit, as coarser grains containing exsolution blebs of alabandite, galena and pyrrhotite.

3.5.6 Mineralogy and Textures: A3 Unit

Unit A3 is significantly poorer in sulfides and is characterized by the presence of manganiferous carbonate and garnet with minor quartz, amphibole and pyroxene/pyroxenoid. Borehole log information that was made available by Vedanta to *Poignant-Molina* showed that the contact between the A3 unit and the B1 unit is at 110.4m depth. The sampling of the GVD038 borehole was terminated before this unit was reached. However due to the gradational contact between the A3 and B1 unit, samples the lowermost samples of the previous unit (44A, 44B and 44C) show some of the mineralogical features that are characteristic of the A3 unit.

The A3 unit contains Mn-rich carbonate in addition to other gangue minerals. Andradite is the most common garnet species in this unit. The gangue minerals recorded deformation and low temperature alteration, in the form of fine-grained kaolinite being present in parts of the section. The deformation is presented as fracturing and micro-scale sigmoidal deformation structures overprinted with fine-grained pyrite in garnet.

The sulfides in this unit are disseminated and fine- to coarse-grained, and are often found as interstitial minerals or micro-fracture filling. The dominant sulfide phases are pyrite, alabandite and sphalerite. Alabandite is even more abundant than sphalerite in this unit. Sulfide aggregates are often recrystallized, showing 120° grain boundary triple junctions, and often exhibit well-developed overgrowths. These features suggest textural re-equilibration. Corroded textures may be interpreted as replacement effects.

3.5.7 Stratigraphic overview

Following his petrographic analysis, *Poignant-Molina (2017)* constructed a detailed stratigraphic column of drillhole GVD038 containing mineralogical and textural features that provides an excellent overview of the stratigraphy of the Gams Formation in the West orebody (Figure 14). This stratigraphy will also be used for the geochemical profiling in the following chapter.

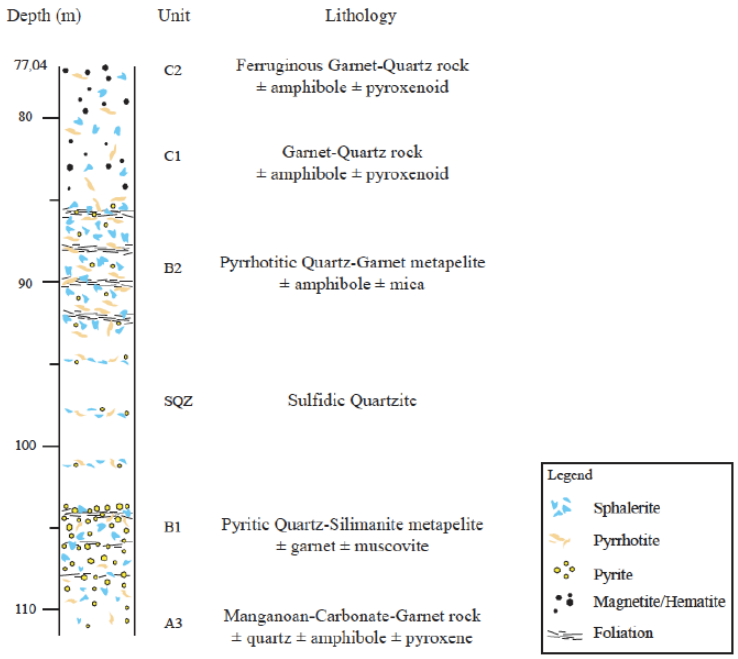

Figure 14: of the Gams Formation in the West orebody from the GVD038 drillhole based on the logging and petrographic analysis of Poignant-Molina (2017) (from Poignant-Molina (2017).

4 Geochemistry

4.1 Background on sulfide mineral geochemistry

4.1.1 Sphalerite

Sphalerite (ZnS) is the primary zinc sulfide ore mineral found in base-metal deposits. The formation of base-metal deposits involves a combination of a wide range of environmental settings and genetic processes. These include the sea floor on which the ore is deposited, faults in the underlying strata from which the metal-rich hydrothermal brines are derived, etc. as well as possible secondary alteration by metasomatism. All these processes and environments bring along a large range of minor and trace elements, which can be incorporated in the crystal structure of the sphalerite. The incorporation of other elements in the crystal lattice is predominantly facilitated by substitution of Zn^{2+} with other divalent ions (e.g. Fe^{2+},Mn^{2+},Cd^{2+},Co^{2+}) as well as by coupled ionic substitutions (e.g. $Cu^{+} + In^{3+}$) (*Deer et al., 1962; Cook et al., 2009; Ye et al., 2011*). The most common substitutes for Zn in sphalerite are iron, manganese and cadmium, with the most common being iron which has concentrations in sphalerite covering a range from merely trace levels to exceeding 15-wt% (*Deer et al., 1962*). Cadmium and manganese concentrations generally range from trace levels to about 4-5 wt%. The upper limit for manganese substitutions in sphalerite is approached at approximately 7-mol% MnS (±6.3wt%), above which MnS incorporation in the sphalerite mineral structure cannot be further accommodated and formation of alabandite occurs (*Cook et al., 2009*). In some

cases trace levels of Hg, As, Tl, Ga, In and Co can be found in sphalerites (*Deer et al., 1962; Cook et al., 2009*)

4.1.2 Alabandite

Alabandite is a rare mineral with an isometric crystal structure and is dimorphic with rambergite (MnS, hexagonal). Alabandite is commonly restricted to Mn-rich sedimentary rocks (both metamorphosed and non-metamorphosed) (*Mücke et al., 1999; Olivo and Gibbs, 2003*), but may also be found in base-metal substitute deposits in carbonate sequences (*Hewett and Rove, 1930*), mesothermal veins in pyritic sedimentary rocks (*Graham, 1978*) and Ag-rich volcanic-hosted epithermal deposits (*Hewett and Rove, 1930*). The rarity of Alabandite can be ascribed to the very small range of Eh-pH conditions under which it is stable in the Mn-C-S-O-H system (Figure 15) (*Mücke et al., 1999*). Iron may be present as a minor element substituting for manganese in alabandite, with documented concentrations of 6.9-10.4 wt% Fe (*Hurai and Huraiová, 2011*).

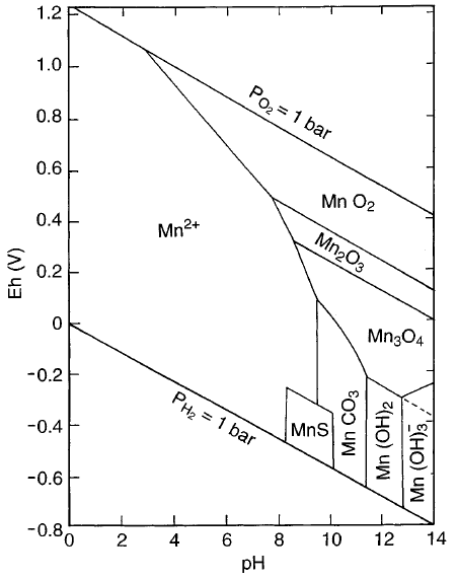

Figure 15: Eh-pH diagram for the system Mn-C-S-O-H at 25°C and 1 bar. Assumed activities for dissolved species are: Mn = 10^{-6}, C,S = 10^{-3} (from Mücke et al. (1999), modified from Brookins (1987)).

4.1.3 Fe-sulfides

The Fe-sulfides that were found in the GVD038 drillhole include pyrite (FeS_2) and pyrrhotite ($Fe_{1-x}S$) with $x = 0$ to 0.2. Pyrite is the most common sulfide mineral found on the earth's surface, whereas pyrrhotite group minerals are very common in mantle rocks and are probably the most common sulfides present in the bulk earth (*Rickard and Luther, 2007*). Pyrite is commonly associated with marine sediments that were deposited under anoxic conditions, and may be present in most marine sediments and rocks in at least trace quantities. Pyrite forms during shallow burial via the reaction of iron minerals with H_2S, which

in turn is produced by the bacterial reduction of dissolved sulfate present in the depositional environment. As an intermediate step to pyrite formation, the Fe-bearing minerals first react with H_2S to form FeS, which then in turn reacts with H_2S to form pyrite, as is shown in Figure 16 (*Berner, 1984*).

Similarly to sphalerite and alabandite, variations in the pyrite chemistry are facilitated by substitution of the divalent main cation (Fe^{2+}) with other minor and trace elements. Common minor elements in pyrite include As (up to 9.6 wt%), Co (up to 2.2 wt%), Sb, Au and Ni. A host of trace elements can be found in pyrite minerals, including: Bi, Cd, Hg, Mo, Pb, Pd, Pt, Ru, Se, Te, Tl and Zn. Finally Ag, Cu and Sn may also be present as minor elements in pyrite, but are typically found within distinct mineral inclusions (*Abraitis et al., 2004*).

Pyrrhotite exists in monoclinic and hexagonal variants (dependent on the Fe content) which are often found together naturally in two-phase mixtures, and may contain Cu, Co, Mn and Ni as trace elements (*Arnold, 1967*). Pyrrhotite and FeS are considered metastable (*Berner, 1984*) and are generally not expected to survive over long periods in geological time. The environmental geochemical controls on the formation of FeS are the organic carbon content (TOC) and reactive iron content. Low TOC and abundant Fe allow for rapid removal of reduced sulfur (in the form of H_2S) from the system, halting the pyritization of intermediate iron sulfides (Figure 16) and allowing for the preservation of these metastable iron sulfides (*Kao et al., 2004*).

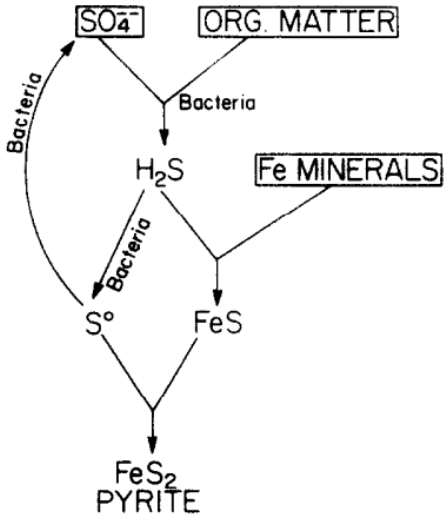

Figure 16: Schematic overview of the process of sedimentary pyrite formation (from Berner (1984)).

4.2 Background on sulfur isotope fractionation

Now that the cationic aspects of the sulfide minerals have been covered, the chemistry of their common anion, sulfide, will be discussed. Sulfur has 25 known isotopes, four of which are stable: ^{32}S (95.02%), ^{33}S (0.75%), ^{34}S (4.21%), and ^{36}S (0.02%). The ratio between these isotopes may be affected by isotope

fractionation processes that cause these ratios to deviate from their respective natural relative abundances. These processes include kinetic fractionation and equilibrium fractionation, among others. In a simplified sense, kinetic fractionation processes separate stable isotopes by their mass during unidirectional processes, whereas equilibrium fractionation processes cause a partial separation of isotopes between two or more substances in a chemical equilibrium. Different geological processes, environments and sources result in sulfur fractionation in different ways, generating a wide variety in the sulfur isotope distribution in nature (Figure 17).

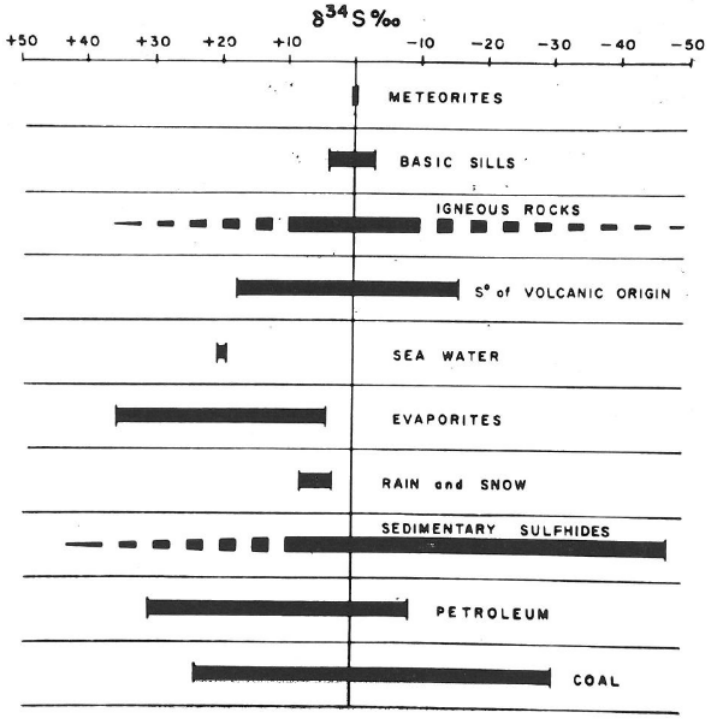

Figure 17: The sulfur isotope distribution in nature. Values are relative to VCDT (from Thode (1970)).

It is important to note that (1) any δ^{34}S values mentioned here are normalized to the internationally recognized standard Vienna Canyon Diablo Troilite (VCDT) and (2) that the degrees of fractionation associated with a fractionation processes discussed below do not take in account the isotopic composition of the parent sulfur, which itself may be fractionated relative to VCDT, causing a shift in the final isotopic composition observed in rocks which is the product of the various fractionation processes involved as well as the isotopic composition of the parent sulfur.

To account for the isotopic composition of the parent sulfur in SEDEX deposits, the age of the SEDEX deposit has to be correlated against this point in history in the evolution of the isotopic composition of oceanic sulfate, from which the sulfur in SEDEX deposits is generally derived. The evolution of the

isotopic composition of sulfate is shown in Figure 18.

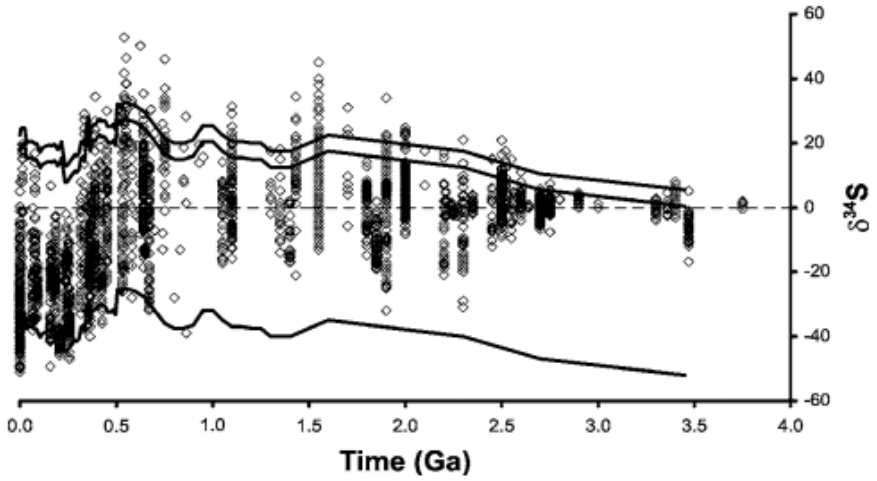

Figure 18: The evolution of the isotopic composition of sedimentary sulfides (diamonds) and sulfate (upper line) through time. For clarity, the isotopic composition of sulfate is also plotted offset by 55% (lower line). (from Canfield (2005)).

4.2.1 Microbial sulfate reduction

As described before sulfide (S^{2-}) is generally introduced in the environment by dissimilatory sulfate (SO_4^{2-}) reduction processes. Sulfate reducing microorganisms (SRM) comprise a group of both bacteria and archaea species which can preform anaerobic respiration using sulfate as an electron acceptor, reducing it to H_2S with SO_3^{2-} as an intermediary species. In one of the more basic models this process can be broken down in four main steps:

1. The uptake of sulfate by the microorganism
2. The reaction with sulfate with ATP (adenosine triphosphate) to form APS (adenosine-5'-phosphosulfate)
3. The reduction of APS to sulfite (SO_3^{2-})
4. The reduction of sulfite to sulfide

Contained within this seemingly straightforward reaction (Although it has to be noted that actual pathways may be more complicated and may vary between SRM species (*Widdel and Hansen, 1992*)) is the fact that not all sulfur is treated equally (*Thode, 1970; Thode, 1991; Habicht and Canfield, 1997*).

During microbial sulfate reduction kinetic fractionation processes take place during some of the various steps involved. These are the steps where the bonds between sulfur and the other elements in the sulfate ions and other intermediate substances are broken. These steps include step 3 and 4 where S-O bonds are broken in the reduction from APS to sulfite and from sulfite to sulfide, resulting in $\delta^{34}S$ fractionation values of $\pm$ 25‰ for each step (*Habicht and Canfield,*

1997; Rees, 1973). Slightly lower values of 10 to 15‰ have also been assigned to step 3 by some authors (*Chambers and Trudinger, 1979*). Minor fractionation of ± 3‰ at most occurs during step 1, the uptake of sulfate by the microbe. The reverse reactions of steps 1, 2 and 3 are assumed to cause no fractionation (*Habicht and Canfield, 1997; Thode, 1991; Rees, 1973;*).
The reason why the strongest isotope fractionation occurs during these bond-breaking steps is the difference in bond energy between these isotopes. Generally lighter isotopic species have lower bond energies and are therefore more favorable for organisms from a net energy gain perspective. Moreover, the lower bond energy in the lighter ^{32}S isotopes result in a faster reactions compared to ^{34}S (*Thode, 1991*). Another major controlling factor on the magnitude of fractionation by microbial dissimilatory sulfate reduction is the rate of reaction, which shows an inverse relationship with the degree of fractionation. The highest fractionations occur when the metabolic rates of sulfate reduction are low, and decrease as the metabolic rate increases with fractionation approaching the limit of 0‰ at high metabolic rates (*Harrison and Thode, 1958*).

In recent years more complex models were proposed for dissimilatory microbial sulfate reduction. These were needed to account for observed $\delta^{34}S$ values lower than -46‰, which is the maximum amount of fractionation associated with the Rees-model (*Brunner and Bernasconi, 2005; Rees, 1973*). *Canfield and Thamdrup (1994)* proposed variation of the basic model in which sulfides produced by sulfate reduction are oxidized to elemental sulfur, which in turn is disproportionated to sulfide and sulfate. The new sulfate can then again be reduced by dissimilatory microbial sulfate reduction. This cycling process results in increasingly depleted sulfide and can be repeated multiple times. *Brunner and Bernasconi (2005)* proposed a revision of the Rees-model in which the fractionation factors associated with the sulfite-sulfide step are revised and incorporates new new forward and reverse steps in the reduction of sulfite to sulfide, allowing for fractionation up to -70‰.

Besides dissimilatory sulfate reduction microorganisms may also convert sulfate to sulfide using assimilatory sulfate reduction, which is a strictly unidirectional process that only results in relatively limited fractionation ranging from <1 to 4.4‰. Moreover the quantity of sulfur that is reduced by means of assimilatory sulfate reduction is several orders of magnitude smaller compared to the quantity that is reduced by dissimilatory sulfate reduction (*Thode, 1991*).

The product of microbial dissimilatory sulfate reduction is an H_2S species that is enriched in ^{32}S and depleted of ^{34}S compared to the relative abundances of these isotopes in nature. The sulfate that remains in the environment will be isotopically heavier as a result of reverse reactions reintroducing sulfate that is now enriched in ^{34}S and depleted of ^{32}S back into the environment. Fractionation relative to the isotope signature of the parent sulfate varies between -15 to -65‰ (*Machel et al., 2005*).As has been mentioned before, the main source of sulfide found in SEDEX deposits is sulfide that has been produced as a result of microbial sulfate reduction. Now that we know that this sulfide hosts an isotopic signature, any variations in the S isotope signature throughout the stratigraphy may be attributed to changes in environmental parameters that affect S isotope fractionation by microbial sulfate reduction, allowing us to constrain some of

the dynamics involved in the evolution of the depositional basin through the stratigraphic history.

4.2.2 Thermochemical sulfate reduction

Thermochemical sulfate reduction (TSR) has only recently received more attention and produces ^{34}S-depleted sulfide as well. The basic reaction under which TSR takes place is:

$$SO_4^{2-} + CH_4 \rightarrow H_2S + CO_3^{2-} + H_2O$$

Significant TSR is associated with higher-temperature environments with temperatures between 80-100°C on the low end and 150-200°C on the high end (*Machel et al., 1995; Machel, 2001*), or possibly even higher temperatures up to 350°C (*Anderson and Thom, 2008*). TSR is thermodynamically possible at temperatures as low as 25°C. Reaction rates at such low temperatures, however, are so low that they are geologically insignificant (*Machel, 2001*).

The rate of TSR is one of the least well understood aspects of TSR, but is dependent on the initial total S concentration, metal complexes, organic acids, the catalytic action of metals: $Ni^{2+} > Co^{2+} > Mn^{2+} > Cu^{2+} > Fe^{2+} > Ca^{2+} = Mg^{2+}$; and the presence of various organic compounds, among other dependencies (*Machel, 2001*). The effects of these environmental parameters on the rate of TSR are still very poorly constrained, with the exception of temperature which shows a clear positive relationship with the rate of TSR (*Machel, 2001*).

4.2.3 Environmental controls on isotope fractionation

One of the environmental controls on the fractionation of S isotopes is the sulfate concentration. Sulfate concentrations below $200\mu M$ show a significant reduction in the magnitude of fractionation with values not exceeding +10‰. The most pronounced effect of sulfate concentration on S fractionation, with fractionation increasing as the sulfate concentration increases, exists with sulfate concentrations in the range of $100\mu M$ to $1000\mu M$, above which the effect becomes less pronounced (*Habicht et al., 2002*). Such low concentrations, however were mostly present in the Archean oceans before 2.4Ga. Sulfate concentrations rapidly increased since, exceeding $1000\mu M$ by the end of the Paleoproterozoic and reaching concentrations going up to 28mM in modern oceans (Figure 19) (*Kah et al., 2004; Habicht et al., 2002; Canfield, 2004; Canfield and Farquhar, 2009; Horita et al., 2002*).

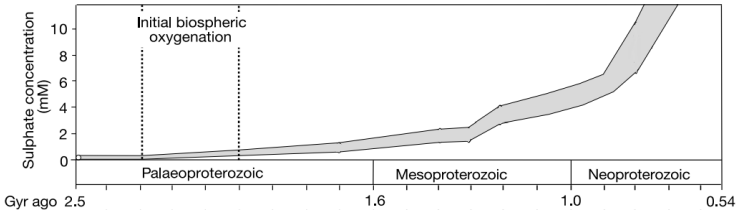

Figure 19: The evolution of the global oceanic sulfate concentration throughout the Proterozoic. Oceanic sulfate concentrations are shown to not exceed 1mM until 1.7Ga and show a rapid increase after 1.3Ga (Modified from Kah et al. (2004)).

Another major environmental control on sulfur isotope fractionation is temperature. Microbial sulfate reduction and TSR both occur at distinct temperature ranges. Sulfate-reducing microbes are known to be generally active at temperatures between 0 and 60-80°C and pH values between 5 and 9.5 (*Seal, 2006; Machel et al., 1995; Machel, 2001*). Thermophile microbes may be active with temperatures up to 110°C (*Machel, 2001*). Above these temperatures microbial metabolism ceases and TSR rates have increased sufficiently to produce geological significant levels of fractionated sulfides (*Machel, 2001*). δ^{34}S levels produced by TSR increase as temperature increases. The degree of fractionation relative to the parent sulfate produced by TSR varies in nature from -20‰ at 100°C to -10‰ at 200°C (*Machel et al., 2005*).

The last major environmental control on isotope fractionation is the openness of the system in which the fractionation occurs. Because δ^{34}S values observed in sedimentary rocks depend heavily on the isotopic composition of the parent sulfate in the environment, the rate of replenishment of sulfate in the environment relative to rate of sulfate reduction is of significance importance. Sulfate reduction depletes the seawater of ^{32}S, causing the sulfate to become isotopically heavier. In a closed or semi-closed system the water is not replenished fast enough with sulfate that has an isotopic composition resembling global seawater, causing the isotopically heavy sulfate to fractionate over and over again, further increasing its δ^{34}S value over time following the Rayleigh fractionation mechanism (*Strauss, 1997*). This increase of δ^{34}S over time in the parent sulfate causes daughter sulfides to become increasingly isotopically heavy as well as time progresses (Figure 20). This produces a predictable pattern throughout a stratigraphy with the oldest units being isotopically the lightest, and younger units becoming progressively isotopically heavy. In an open system the isotopic composition of the parent sulfate is significantly more stable, following global trends.

4.3 Sulfur isotope data from other SEDEX deposits

To better place the sulfur isotope data from the Gamsberg Zinc deposit in context, comparisons may be drawn between δ^{34}S found in the Gamsberg Zinc deposit and those found in other SEDEX deposits from around the world.

A sulfur isotope study on the sulfides in the Broken Hill deposit, New South Wales, Australia revealed δ^{34}S values ranging from -3.3 to +6.7 per mil and are interpreted to result from either a mixed sulfur source, combining sulfide derived from inorganically reduced sulfate as well as magmatic sulfur, or sulfur derived from biogenically reduced sulfate (*Spry, 1987*).

Dixon and Davidson (1996) found a wide variety in δ^{34}S values between different minerals and different geological and litholocial units. In the Dugald River Zn-Pb deposit (Australia) they found average δ^{34}S values of 1‰ in sphalerite and pyrite minerals the south of the deposit, coinciding with the highest Cu concentrations in the ore. The northern part of this ore shows values of 8‰. The adjacent footwall and hangingwall, however, show no zonation in δ^{34}S values, which peak around 3-4‰, but go as low as -14.5‰. Overlying dolomites show another extreme, with pyrite grains in this unit having δ^{34}S values that

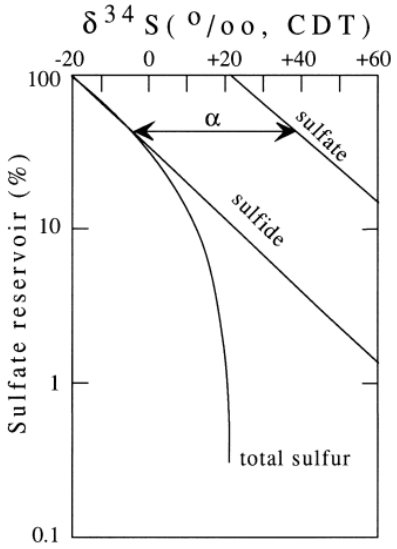

Figure 20: Schematic evolution of the sulfur isotopic composition following the Rayleigh fractionation mechanism (α = fractionation factor) Values are relative to VCDT (from Strauss (1997)).

range from +5.5 to +17.5‰. The large variation between populations is attributed to varying degrees of closed-system biogenic sulfate reduction. The source of the sulfur, however, is interpreted as TSR by these authors based on mass-balance calculations, δ^{13}C values, high temperatures involved in the ore formation and the trend toward oceanic δ^{34}S values.

Leach et al. (2005) argued in their paper on sediment-hosted Zn-Pb deposits that the mechanisms from which reduced sulfur is derived in BHT deposits change over time and with increasing temperature from BSR to TSR.

4.3.1 Sulfur isotopes form SEDEX deposits in the Aggeneys-Gamsberg district

Several authors (*McClung et al., 2007; McClung et al., 2010; von Gehlen et al., 1983; Foulkes, 2014*) have recorded sulfur isotope data of the several inselbergs in the Aggeneys-Gamsberg district, including but not limited to the Gamsberg deposit:

- *McClung et al. (2007)* recorded δ^{34}S for barites in the Swartberg, Tank Hill, Big Syncline and Gamsberg deposits, and made a summary of δ^{34}S values found in primary sulfides from the Swartberg, Broken Hill, Big Syncline and Gamsberg deposits.
- *McClung et al. (2010)* recorded δ^{34}S values for both sulfides and barites in the Swartberg, Broken Hill and Big Syncline deposits.
- *von Gehlen et al., (1983)* recorded δ^{34}S values for barites and sulfides in the Swartberg, Broken Hill, Big Syncline and Gamsberg deposits.

- *Foulkes (2014)* recorded δ^{34}S values for sulfides in the Gamsberg deposit.

The results of these studies were compiled by *Foulkes (2014)* and shown in Figure 21. An increasing gradient in δ^{34}S is seen from the westernmost unit (Swartberg/Black Mountain) towards the easternmost unit (Gamsberg). These were interpreted as a proximal relation with the source of the hydrothermal brines involved in forming these SEDEX deposits, with the Swartberg deposit being the most proximal to the locus of the hydrothermal vent and Gamsberg being the most distal (*McClung et al., 2007*). The sulfates (barite) and sulfides both express this general trend which may indicate that the sulfur in both the sulfates and the sulfides is derived from a common seawater source (*Foulkes, 2014*).

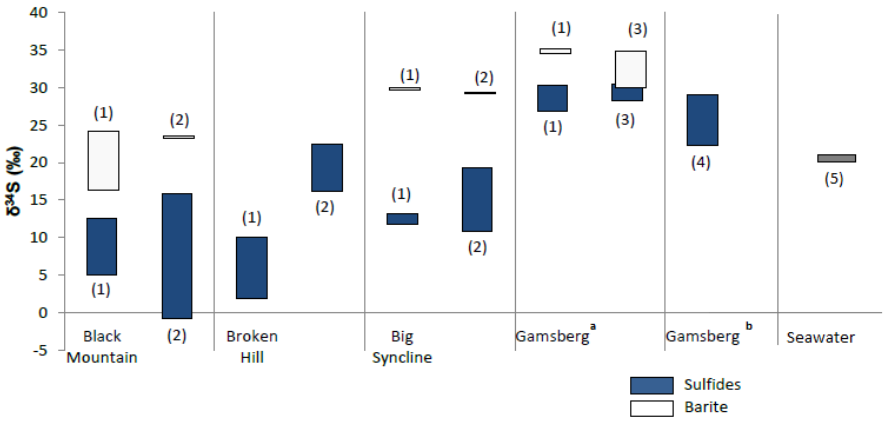

Figure 21: Compilation of δ^{34}S values (‰) for sulfides and barite from samples from Black Mountain, Broken Hill, Big Syncline and Gamsberg, as well as the global seawater S isotope composition at 1.6Ga. Gamsberg^a denotes compiled literature values from sources $_{1-3}$; Gamsberg^b represents data from Foulkes (2014). Sources: (1) von Gehlen, (1983); (2) McClung et al. (2010); (3) McClung et al. (2007); (4) Foulkes (2014); and (5) Figure 18 from Canfield (2005). (Adapted from Foulkes (2014)).

5 Results

5.1 LA-ICP-MS Analysis: Qualitative and quantitative approach

Two sets of sulfide minerals were analyzed in the 34 polished samples, with duplicate analysis being performed on all of the samples in order to obtain a statistically robust dataset, with the exception of sample GVD26A which underwent triplicate analysis. The LA-ICP-MS analyses were performed for 2 minutes per analysis. During the first minute a blank signal was measured, after which the laser excimer was turned on and the sample itself was measured. The average blank signal was later subtracted from the sample measurements. Each sample analysis was bracketed by analyses of a reference material with a known isotopic composition, Mass-1. The compartment that contains the samples during analysis only allows for two samples and up to two reference materials. So

after each duo of samples was replaced by a new set of two, the reference material was measured first.

The measurements themselves were carried out using a spot size of 120μm in nearly all the samples, with a spot size of 80μm being used in cases where minerals were too fine grained. An analysis of the effect of spot size on the precision of the produced data is shown in Figure 22. Spot sizes of 60-120μm are preferred, spot sizes of 30-40μm are acceptable but not preferred and require more analyses for statistical robustness. Spot sizes of 20μm and lower show very significant relative standard deviations, which increase to extreme proportions as spot size decreases, rendering them unusable.

Other analysis parameters are listed in Table 1. These values were largely

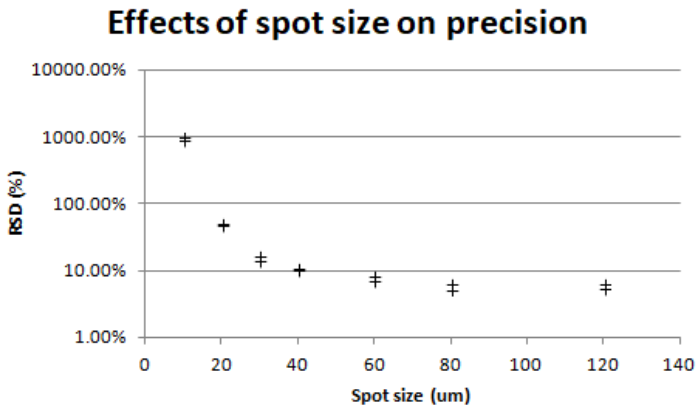

Figure 22: The effect of spot size on precision expressed in relative standard deviation (RDS; %). Duplicate analyses were performed for all spot sizes available for the excimer laser, with the exception of 5μm as the progressively smaller analyses showed an exponential increase in deviation. Note the logarithmic scale of the vertical axis.

adapted from previous authors who measured sulfur isotopes or performed elemental analyses with the same brand and type of ICP-MS. From there several analysis parameters including settling time, sample time, number of peaks per sample, the search window and the integration window were adjusted whilst measuring the same reference material (Mass 1) in order to obtain the lowest relative standard deviation.

Data processing was performed by first determining the timeframe of blank measurements in the exported files and from this timeframe determine the average blank signal for ^{32}S and ^{34}S. The blank timeframe lasts from the start of the analysis until a few measurements before the start of the laser ablation. This blank signal was subtracted from the measurements, after which the ^{34}S/^{32}S ratio was determined for each measurement. The timeframe for sample measurements was defined around 5-10 measurements after laser ablation started in each analysis to allow for re-stabilization of the plasma and to omit these unstable measurements from the produced results.

Mason et al., (2006) investigated the effects of ablation time and the crater depth/diameter ratio on $^{34}S/^{32}S$ in sulfide minerals when making a single crater and concluded that no significant change in $^{34}S/^{32}S$ occurs as a result of these factors during laser ablation analyses. These conclusions were confirmed in this study with a random sample of 4 mineral analyses and 4 reference material analyses where the change in the $^{34}S/^{32}S$ through time during an analysis was quantified. This test revealed that during an analysis the first-order $^{34}S/^{32}S$ ratio changes up to a few percent from beginning to end in both the sample- and reference material analyses. When comparing these results with the instrumental mass bias drift between these analyses and bracketing analyses, which is further discussed in the next section, most of these changes through time can be attributed to instrumental mass bias drift.

General setup	
Rf power	1400 W
Sample gas flow rate	0.88 L/min
Ar cooling gas flow	16.0 L/min
Ar auxiliary gas flow	0.8 L/min
Additional gas flow	1.063 L/min
Sampling and skimmer cones	Nickel
$m/\Delta m$	4000
Parameters for isotopic measurements	
Mass window	150%
Settling time	1 ms
Sample time	10 ms
Number of samples per peak	10 (^{32}S)
	30 (^{34}S)
Runs and passes	200x1
Analysis time	2 min
Replicate measurements	2
Search window	50%
Integration window	80%
Acquisition mode	Escan
Detection mode	Counting

Table 1: Operating parameter settings for the ThermoFischer Scientific Element 2 magnetic sector ICP-MS optimized for sulfur isotope measurements using laser ablation

5.1.1 Instrumental mass bias correction

Due to a variability of the transmission of the ion beam in the mass spectrometer over time accuracy and external precision of the produced data is affected strongly. Due to this instrumental mass bias, produced results may vary significantly from their true values. This calls for the need of a mass bias correction. Mass bias correction is performed by normalizing measurements to the known

isotopic value of a reference material using a generalized power law:

$$R_{true} = R_{measured} * f^{(M_2 - M_1)}$$

With R_{true} being the true ratio between measured isotopes, $R_{measured}$ being the measured ratio between measured isotopes, f is the mass fractionation coefficient and M_1 and M_2 are the masses of the measured isotopes.
The mass fractionation coefficient, f, is generally calculated using multiple isotope couples which combined in a single scatter diagram with one axis showing the natural logarithm of the ratio between the true and measured isotopic ratios, and the other axis showing the natural logarithm of the mass ratio for these isotope couples, with the slope of the resulting line being the mass fractionation coefficient (e.g. *Rodushkin et al., 2016*; Figure 23).

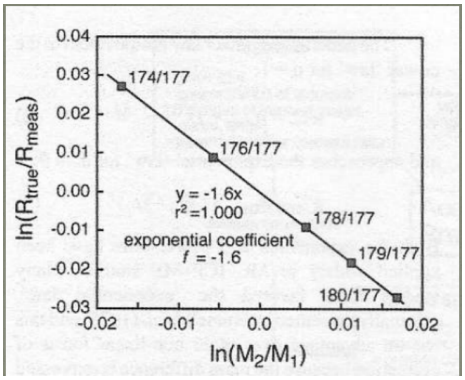

Figure 23: An example of regression lines obtained by mass bias evaluation. The horizontal axis shows the ratio between masses of different isotope pairs. The vertical axis shows the ratio between the known and measured isotopic ratios of the respective isotope pairs. The slope of the regression line is the mass fractionation coefficient which can be used to correct for the instrumental mass bias. (From Simonetti (2012))

This study, however, used a simplified version of the mass bias correction, using only the observed and known $^{34}S/^{32}S$ ratios. The known value of this ratio was set at 0.045268 which corresponds with the $\delta^{34}S$ value of +5.85‰ relative to VCDT reported by *Fu et al., (2016)*. The formula then simplifies to:

$$R_{true} = R_{measured} * F$$

Where F is the *mass bias correction factor*. This factor was calculated for each reference material analysis in order to evaluate the internal drift of the apparatus and correct for it. A correction was applied by simply multiplying the observed isotope ratio with the determined mass bias correction factor. The mass bias correction factor for the samples themselves was determined by means of linear interpolation of the values for F observed in the reference material analyses that directly precede and follow a sample measurement.

5.2 LA-ICP-MS Analysis: Results

After the mass bias correction was applied to all measured samples, the corrected $^{34}S/^{32}S$ ratios were converted to $\delta^{34}S$ values relative to VCDT. The duplicate and triplicate analyses for each sample were combined into a single dataset per sulfide mineral suite, from which the average isotopic fractionation was calculated. Finally the isotopic composition of each sample in the form of $\delta^{34}S$ values was plotted against their stratigraphic depth for both of the two mineral suites. Plots were created showing both the average results for each sample as well as the individual analyses per sample and the standard deviation between those duplicate analyses. The two sets of sulfide minerals that were analyzed include a sphalerite- and an Fe-sulfides set.

5.2.1 Fe-Sulfides data

The Fe-Sulfide dataset was acquired on April 16-18 2018. The Fe-sulfides that were analyzed are pyrite and pyrrhotite which are the dominant iron sulfides in the GVD038 drillhole. Because the abundance of these minerals relative to each other changes throughout the stratigraphy, both minerals were incorporated into a single dataset to have data from sufficiently homogeneous mineral grains of sufficient size throughout the whole stratigraphy. The compiled $\delta^{34}S$ data for the iron sulfides against stratigraphy is shown in Figure 24.
The isotope data from the iron sulfides shows significant variability throughout the stratigraphy. Negative $\delta^{34}S$ values around -9‰ are observed in the lower part of unit A3. Towards the top part of unit A3 $\delta^{34}S$ values increase to +10 to +20‰ in unit B1. At the top of unit B1 $\delta^{34}S$ values increase to +30 to +55‰ into the sulfidic quartzite unit (SQZ). The SQZ unit shows a particularly interesting feature in the form of a significant drop of about 30‰ in $\delta^{34}S$ around 100m depth. Above this dip more stable $\delta^{34}S$ values around +40‰ are observed a zone spanning from the top of the SQZ unit up to unit C2, with the exception of a positive spike going up to +60‰ in unit B2.

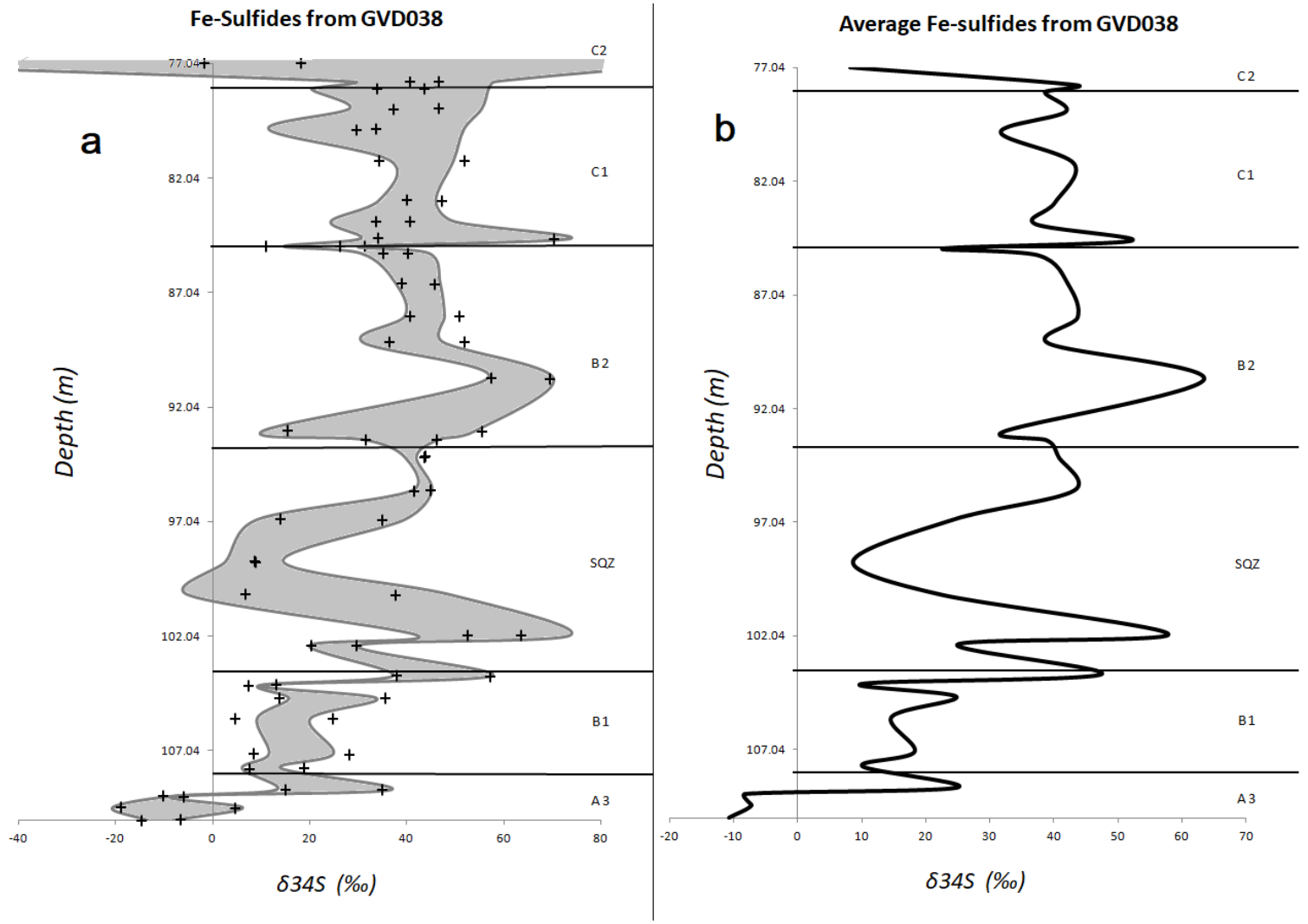

Figure 24: Recorded S isotope data of iron sulfides pyrite and pyrrhotite from the 34 samples of drillhole GVD038 from Gamsberg.δ^{34}S values are normalized to VCDT and plotted against stratigraphic depth. The various members of the Gams Formation from which these samples are derived are shown on the right hand side. **a)** Crosses represent the average value of an analysis. The gray area represents the standard error between the two analyses for each sample relative to the average value of the combined analyses. **b)** A simple curve showing the average δ^{34}S values for each sample obtained from the combined data of the duplicate analyses.

5.2.2 Sphalerite data

The sphalerite dataset was acquired on May 29-31 2018 using the same equipment and setup as the iron-sulfide dataset. Sphalerite occurs as a major sulfide mineral phase throughout the stratigraphy and it was possible to perform duplicate analyses for sphalerite grains in each of the 34 samples from the GVD038 drillhole. The compiled δ^{34}S data for sphalerite against stratigraphy is shown in Figure 25.

The sphalerite data exhibits a similar general pattern to the Fe-sulfides. Unit A3 shows negative δ^{34}S values fluctuating around 0‰. In the bottom half of unit B1 δ^{34}S values suddenly increase with a significant amount (±30‰). Throughout the top part of the stratigraphy the δ^{34}S values remain relatively constant with only minor fluctuations.
A smaller scale similarity between both datasets are the relatively minor, but nonetheless noticeable spikes in δ^{34}S values at the lithological unit boundaries. Although the first order pattern shows strong similarities between the two mineral types, there are a number of stark differences on a smaller scale and in the general pattern. First of all the δ^{34}S values in the in the C1-SQZ units differ with approximately ±10‰, with the iron sulfides showing values around +40‰ and the sphalerite showing values around +30‰.
Furthermore the Fe-sulfide dataset shows a larger amount of local variability in these units than the sphalerite data. There is a positive spike of +20‰compared to adjacent samples, in the middle of unit B2 in the Fe-sulfide data as well as a large negative spike of -30 to -35‰relative to the adjacent samples, in the middle of the SQZ unit. The spread between the duplicate analyses (Figure 24a), however, has shown that both measurements reflect a spike compared with the units that lay above. The sample that lays directly under this spike however is more ambiguous as the duplicate analyses for that sample show a significant spread which averages out to values reminiscent of the δ^{34}S values found above the spike in unit B2. The same is true for the negative δ^{34}S spike in the SQZ zone which is reflected in multiple samples with duplicate analyses for the bottom of the spike showing little variation between them.
The last major difference between the sphalerite and Fe-sulfides datasets lays in the B1 and A3 units. In the sphalerite data δ^{34}S values remain constant until halfway through the B1 unit, when a sudden drop occurs where δ^{34}S values decrease with ±30‰ to values around 0‰. In the Fe-sulfides dataset this drop occurs in two phases. At the top of the B1 unit δ^{34}S values drop with ±25‰ to values around +15‰. At the top of unit A3 these values drop again with ±25‰ to values around -10‰.

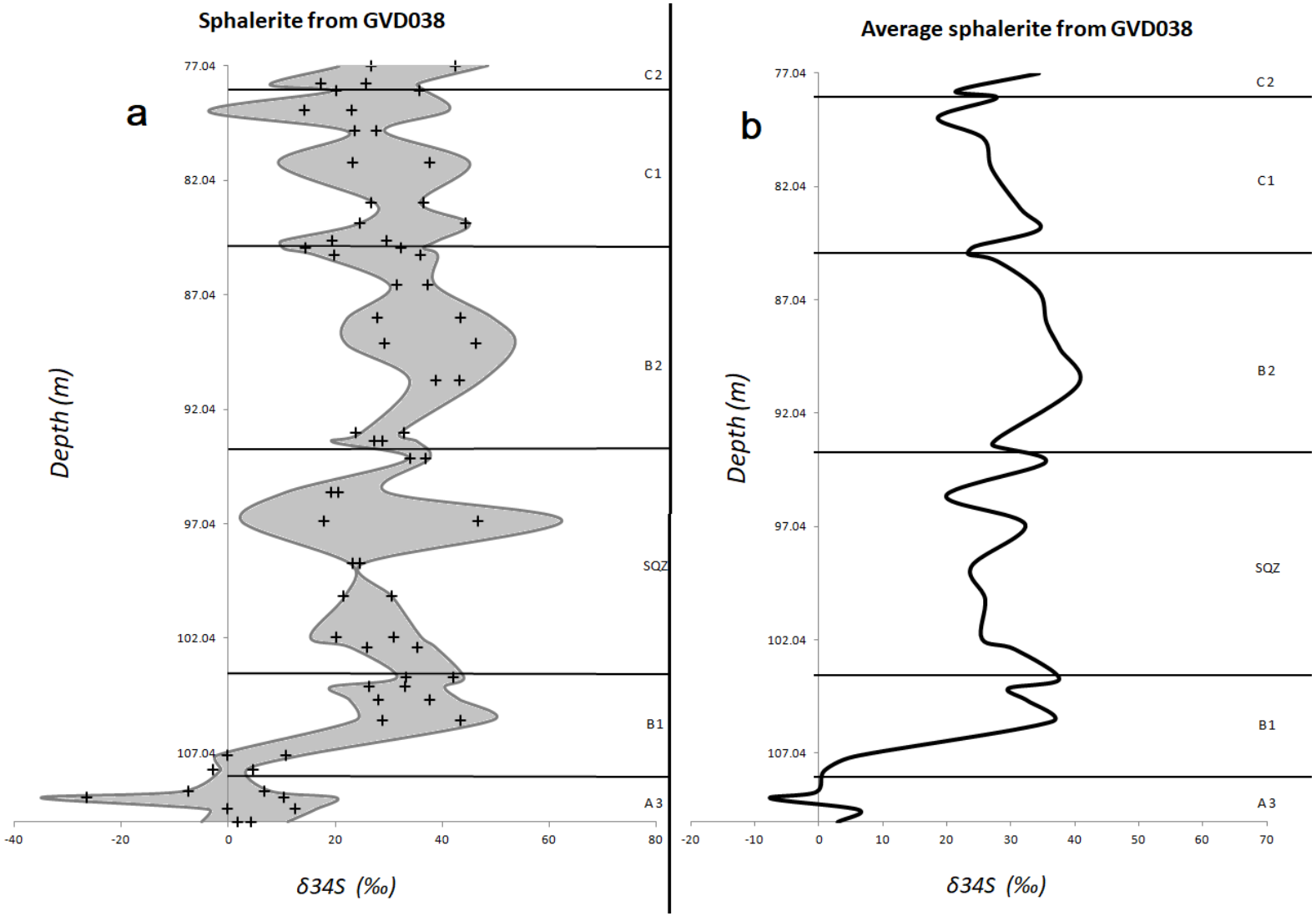

Figure 25: Recorded S isotope data of iron sulfides pyrite and pyrrhotite from the 34 samples of drillhole GVD038 from Gamsberg.δ^{34}S values are normalized to VCDT and plotted against stratigraphic depth. The various members of the Gams Formation from which these samples are derived are shown on the right hand side. **a)** Crosses represent the average value of an analysis. The gray area represents the standard error between the two analyses for each sample relative to the average value of the combined analyses. **b)** A simple curve showing the average δ^{34}S values for each sample obtained from the combined data of the duplicate analyses.

5.3 Comparison with S isotope data from other studies on the Aggeneys-Gamsberg district

Previous studies on S isotopes in the Aggeneys-Gamsberg district have shown that positive δ^{34}S values are found in sulfide minerals throughout this district (Figure 21, *Foulkes (2014)*). Relatively low values are observed in the westernmost deposit, Black Mountain (Swartberg), ranging from -1 to +15‰ (*von Gehlen, 1983; McClung et al., 2010*). Going eastward, the next deposit (Broken Hill) shows more positive δ^{34}S values ranging from +2 to +24‰ (*von Gehlen, 1983; McClung et al., 2010*). The Big Syncline deposit continues the increasingly positive trend, although it has to be noted that the upper limit of δ^{34}S values is slightly lower than found in the previous deposit, only ranging from +10 to +20‰ (*von Gehlen, 1983; McClung et al., 2010*). At the easternmost deposit, Gamsberg, the highest δ^{34}S values were reported by several authors. δ^{34}S values in sulfides range from +23 to +30‰(*von Gehlen, 1983; McClung et al., 2007; Foulkes, 2014*).

Foulkes (2014) provided a detailed study on isotope variability throughout the B unit of the Gams Formation in the North orebody of Gamsberg (Figure 26). S isotope data was obtained from pyrite and sphalerite grains and plotted against stratigraphic depth. As shown in Figure 26, δ^{34}S values in sphalerite grains are the lowest at the bottom of unit B in the North orebody (around +27‰) and increase to stable values of +29 to +30‰. δ^{34}S values in pyrite grains show a similar patter with the lowest values being observed at the bottom of the unit and higher, more stable values being observed above. One exception is a drop of 2‰ at the 192m mark.
The first order S isotope profiles from this dataset are similar to the profiles obtained in this study, with the lowest δ^{34}S values being observed in the bottom of the B unit, and increasing towards stable values towards the top.

Nevertheless there are some significant differences between the S isotope data reported by *Foulkes (2014)* and those obtained in this study:

- The increase in δ^{34}S values from the bottom towards the top of the B unit is significantly less extreme than observed in this study. In this study δ^{34}S values in the B unit increase by a magnitude in the order of +30‰ in the sphalerite- and iron sulfides datasets from the West orebody (Figures 24 & 25), whereas an increase of only +3‰ is reported from these minerals in the North orebody (Figure 26).

- The range of the reported δ^{34}S values in the pyrite and sphalerite grains in the North orebody are very similar with the lowest values laying around +27‰ and the higher values laying around +29 to +30‰ (Figure 26). In the West orebody a significant difference exists between the δ^{34}S values observed in the pyrite and those observed in sphalerite grains. Sphalerite grains at the bottom of the B unit show values of +0‰ and those in the rest of the B unit range from +20 to +40‰ (Figure 25). Iron sulfide grains from the West orebody, on the other hand, show values of +10 to +20‰ at the bottom of the B unit and range from +10 to +65‰ in the rest of the B unit (Figure 24).

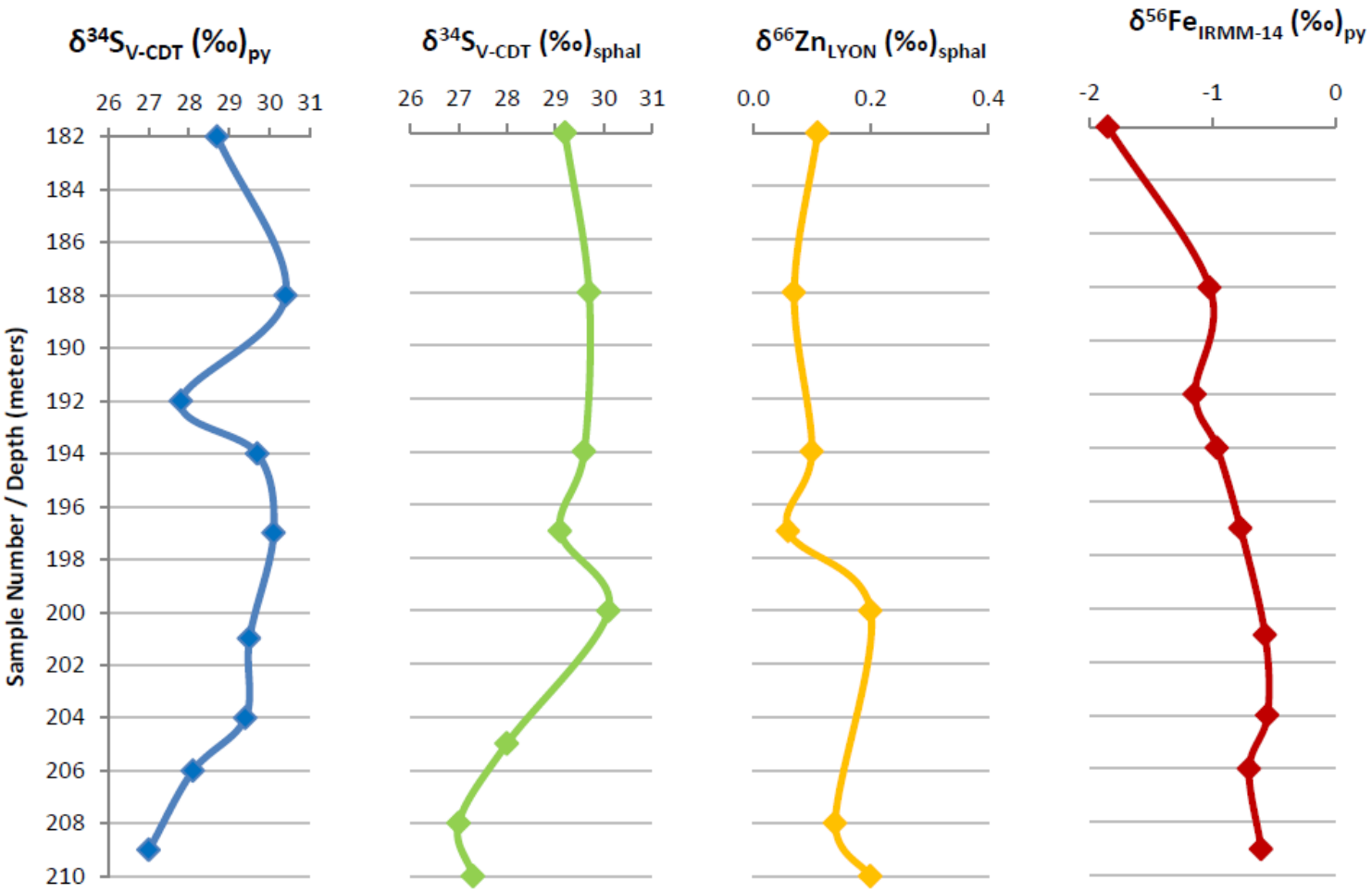

Figure 26: S-, Zn- and Fe isotope data from from the B unit of the Gams Formation obtained from drillhole G1 from the North orebody of Gamsberg. Isotope data is plotted against stratigraphic depth (From Foulkes (2014)).

6 Discussion

6.1 Comparison with sphalerite geochemistry from previous work on drillhole GVD038

When comparing the sulfur isotope data with sphalerite geochemistry obtained from drillholes GAM107 and GVD038 in previous studies (Figures 2, 3 & 27) there does not appear to be a parallel correlation between the sulfur isotope data obtained from the sphalerite population in this study and the base metal abundances reported in the previous assessment of the samples from GVD038 by *Poignant-Molina (2017)*. The large spike in Mn concentrations and Mn/Zn ratios around 95m depth is not reflected in the sulfur isotopic composition of the sphalerite grains.

The general Mn and Mn+Fe patterns (Figure 3) and the Mn/Zn and Mn/Fe patterns (Figure 27A) from the sphalerite population of drillhole GVD038 each show a similar signal, with the manganese content dropping significantly above the C1-B2 border, before stabilizing halfway the C1 unit. As can be seen in Figure 27, a similar trend is not reflected in the S isotope signal from either the Fe-sulfides data, or the sphalerite S isotope data. One could argue that in the sphalerite dataset δ^{34}S values drop slightly in unit C1. However, this drop is very slight and does not significantly differ from δ^{34}S values observed in the SQZ unit. Moreover, the steep rise in δ^{34}S observed in the B1 unit in both the sphalerites and Fe-sulfides is not reflected in the evolution of the sphalerite cationic composition, which is relatively stable throughout the lower part of the stratigraphy.

Whilst the sulfur isotope data does not show a first order correlation with the manganese content in the sphalerite population of these samples, it may provide additional geochemical constraints that give insights in the evolution and dynamics of the depositional environment. The better the parameters involved in the deposition of the Gamsberg zinc deposits are understood, the better a framework can be constructed in which a manganese enrichment process can be fit.

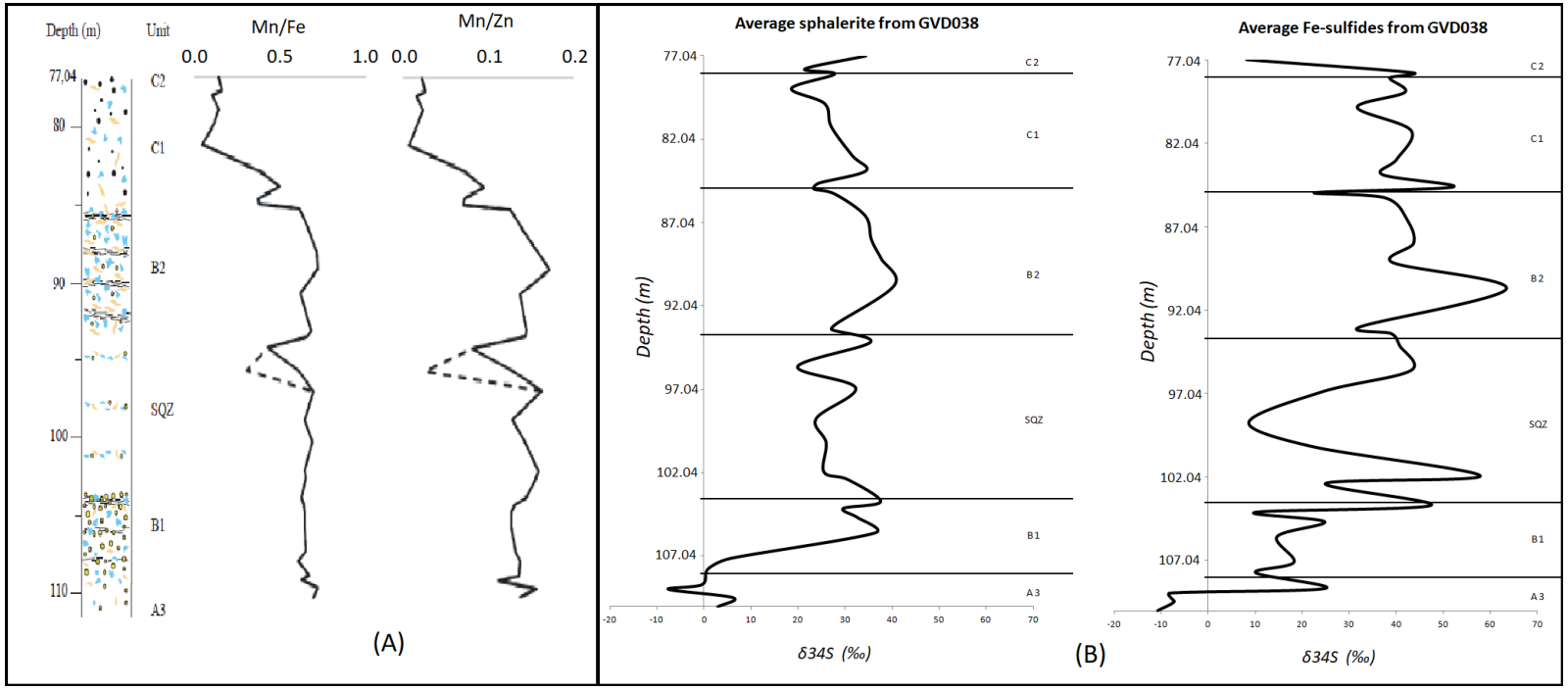

Figure 27: Combined geochemical data from drillhole GVD038. **A:** Mn/Fe and Mn/Zn ratios observed in sphalerite grains from drillhole GVD038 plotted against stratigraphic depth (*Poignant-Molina (2017)*). **B:** δ^{34}S values obtained in this study from sphalerite and iron sulfide grains from the same sample suite from drillhole GVD038 plotted against stratigraphic depth (Mn/Zn and Mn/Fe diagrams adapted from Poignant-Molina (2017))).

6.2 Geochemical constraints

6.2.1 Sulfur isotope data

The isotope data obtained in this study can provide useful insights in the depositional environment and formation of the Gams Formation. The δ^{34}S values from the iron sulfides from the top part of the stratigraphy shows general values around +40‰ with a maximum around +60‰. The δ^{34}S values obtained from sphalerite grains shows general values around +30‰ in all but the bottom part of the stratigraphy, with a maximum around +40‰. When accounting for the isotopic composition of the parent sulfate, the primary mechanism of sulfur fractionation can be constrained.

With the Bushmanland Group being dated at approximately 1.6Ga, these values can readily be correlated with the oceanic sulfate curve from *Canfield (2005)* (Figure 18) when assuming the parent sulfate to have a similar isotopic composition as global oceanic sulfate. The global oceanic sulfate curve shows that oceanic δ^{34}S levels were approximately +21‰ around 1.6Ga. Subtracting this value from the isotopic signal observed in the iron sulfide minerals, shows that the isotopic fractionation relative to seawater values showed positive values around +20‰$_{SW}$ for the younger part of the stratigraphy and values around -30‰$_{SW}$ in the oldest parts of the stratigraphy, with the subscript SW indicating that these values are corrected for the global seawater values present around 1.6Ga. For the sphalerite minerals these values are around +10‰$_{SW}$ for the younger part of the stratigraphy and -20‰$_{SW}$ in the oldest part of the stratigraphy.

However one has to consider if the parent sulfate in the depositional basin indeed reflected global oceanic isotopic values, or rather an enriched sulfate species present in local basins. As shown before in Figure 18, the isotopic composition of barites ($BaSO_4$) in the Aggeneys-Gamsberg district increases from the west to the east, with barites from Gamsberg showing δ^{34}S values of +32.9 ±2.5‰(*McClung et al., 2007; Von Gehlen, 1983*). At Gamsberg, barite can be found in a massive body that overlies stratigraphically equivalent sulfide horizons (*McClung et al., 2007*) If we assume the barite found in the Gamsberg deposit to reflect the isotopic composition of the parent sulfate at the time of deposition, subtracting the average isotopic composition of the barites at Gamsberg, 33‰, from the measured δ^{34}S values results in a more negative isotope signature.
The isotopic composition of the Fe-sulfides is approximately +7‰$_{Barite}$ for the more stable parts of the stratigraphy, dropping to -18‰$_{Barite}$ in unit B1 and dropping further to -43‰$_{Barite}$ in unit A3. The subscript *Barite* indicates that these values have been corrected for the isotopic composition of the parent sulfate.
The isotopic composition of the sphalerite population is approximately -3‰$_{Barite}$ for majority of the stratigraphy when corrected for parent sulfate, sometimes increasing to 0‰$_{Barite}$ and occasionally becoming slightly positive. In the B1 unit values drop to -33‰$_{Barite}$ and finally stay low in the A3 unit fluctuating between -43 to -28‰$_{Barite}$.
Previous studies have shown that precipitation of sulfate minerals only result

in very minor fractionations with values of 0 to +2.4‰ for anhydrite and gypsum relative to the seawater they precipitated from (*Strauss, 1997*). Thus a large difference remains between seawater sulfate levels and the sulfates from the Gamsberg deposit.

The evolution of negative δ^{34}S values around -10 to 0‰ in the oldest part of the analyzed stratigraphy, increasing with time until stable δ^{34}S values around +30 to +40‰ are reached can be explained by closed-system Rayleigh evolution. The Rayleigh fractionation mechanism (Figure 20) describes how in a closed system depletion of ^{32}S in the parent sulfate due to fractionation by sulfate reduction results in the remaining sulfate species becoming increasingly isotopically heavy. Sulfides derived from the residual isotopically heavy sulfate will be relatively depleted in ^{32}S as well. This process results in dissolved sulfate and precipitated sulfides to become progressively isotopically heavy until the total pooled sulfide species reaches the initial isotopic composition of the sulfate. An increase in δ^{34}S values through time, until reaching stable, more positive values is observed in both the Fe-sulfides and sphaleriete populations.The isotopic composition of the sphalerite population above unit B1 shows δ^{34}S values in the order of +30‰ which corresponds with the isotopic composition of the barite population at Gamsberg, +32.9 ‰.
The problems with applying this model, however lay in the co-evolution of the sulfate and sulfur species at Gamsberg and the suddenness of the increase. The isotopic composition of barites from Gamsberg only show limited variability with reported values of +32.9 ±2.5‰, albeit obtained from a limited number of samples (*McClung et al., 2007; Von Gehlen, 1983*), whereas the sulfide species increase with ±35‰ and ±60‰ for sphalerite and the iron sulfides respectively. Furthermore this increase occurs in a matter of only 1 meter in the sphalerites and over two very steep stages within the span of 6 meters in the iron sulfides. However, one may argue that the values encountered at the base of the SQZ are a positive anomaly. Moreover the rates of deposition as well as the size of the depositional sub-basin are not known. Therefore the rate of Rayleigh fractionation remains unknown and this model can not be fully discredited as the primary factor that resulted in the observed δ^{34}S profile.

It is possible nonetheless to come up with a model that can explain both the difference between the isotopic composition of the barites found at Gamsberg and that of global seawater, as well as provide some constraints on the depositional environment. This model involves a closed system in which Rayleigh fractionation occurs on a timescale spanning the formation of all the sulfide ore deposits in the Aggeneys-Gamsberg mining district, rather than the deposition of only the Gamsberg deposit.
As shown before the Aggeneys-Gamsberg district has a wide variation of sulfur isotope values in sulfides and sulfates that increase towards the east (Figure 21). In the Black Mountain deposit, isotope values for barite do match up with global oceanic sulfur isotope composition. As the supracrustal volcano-sedimentary rocks from the Bushmanland Group host all the inselbergs in the Aggeneys-Gamsberg district it is logical to assume these deposits were all located in the same depositional basin. If this was a closed basin, sulfur fractionation will over time have resulted in isotopically heavier dissolved sulfate. Linking the spatial evolution of the isotopic composition of the barites in the Aggeneys-

Gamsberg district to the temporal aspect of the Rayleigh fractionation process it becomes clear that deposition of both sulfate and sulfide minerals started at Black Mountain in the west where isotopic values resemble global seawater, becoming isotopically heavier with subsequent deposits that precipitated further eastward up until the Gamsberg deposit, with only limited isotopic maturation of the parent sulfate occurring during the deposition of Gamsberg itself. This model is backed up by similar interpretations made by *McClung et al. (2007)*.

A second feature that can be better constrained with the new sulfur isotope data is the mechanism of sulfur fractionation. The oldest part of the analyzed stratigraphy shows an isotopic composition with negative δ^{34}S values around -43 to -33‰ in iron sulfides and sphalerites respectively when corrected for parent sulfate levels. These fractionation levels relative to seawater are lower than expected from thermochemical sulfate reduction (TSR), which has associated fractionation levels of a minimum of -20‰ at 100°C, becoming more positve as temperature increases (*Machel et al., 2005*). Microbial sulfate reduction, on the other hand is associated with δ^{34}S values ranging from -65‰ to -15‰. The observed δ^{34}S values of -43 to -28‰$_{Barite}$ are thus lower than values associated with TSR, but fit well within the margins associated with microbial sulfate reduction.
However as the samples at which these lowest δ^{34}S values were observed are at the bottom of the observed stratigraphy, it is uncertain if microbial sulfate reduction is the primary source of reduced sulfate for the full duration of the deposition of the Gams Formation.

The isotopic values found above unit B1, however provide a very different image. These values of +7‰$_{Barite}$ in the Fe-sulfides and -3‰$_{Barite}$ in the sphalerites are more closely associated with fractionation by means of TSR under high temperatures, albeit the Fe-sulfides still show very high values nonetheless. This change from δ^{34}S values as low as -43‰$_{Barite}$ to values around 0‰$_{Barite}$ could mean that the main source of reduced sulfur changed from microbial sulfate reduction to TSR. This can be corroborated by stable oxygen isotope analyses by *McClung et al. (2007)*. δ^{18}O values placed the minimum temperature under which the sulfate that later formed the barite at Gamsberg fractionated at 120°C. However it has to be noted that substantial graphite was observed in the samples from the B1 unit by *Poignant-Molina (2017)*, which is indicative of high metamorphic temperatures as well as the presence of organic material in the pre-metamorphic sediment. The presence of graphite was not reported by *Poignant-Molina (2017)* in overlying units in drillhole GVD038 in his extensive petrographic description of these rocks, but is reported by other authors in the B1 units elsewhere at Gamsberg (*Stalder and Rozendaal, 2004; Foulkes, 2014*). This further backs up the idea that the main source of reduced sulfur produced by sulfate reduction changed from microbial sulfate reduction to TSR in unit B1.

6.2.2 A genetic model for the change of microbial sulfate reduction to TSR as the primary source of reduced sulfur

When taking the petrography of the A3 unit compared to that of the overlying units into account, the apparent paradox of acknowledging TSR and microbial sulfate reduction both as primary mechanisms for reducing sulfur derived from seawater can be unfolded:

- Unit A3 is significantly poorer in sulfide minerals than its successors.
- The oldest part of the sulfide mineralization in the lower B1 unit and A3 unit shows δ^{34}S so low that, if derived from seawater sulfate, it is likely the result of microbial activity.
- The upper B1 unit and overlying units show δ^{34}S values that are more in line with values produced by high temperature TSR.
- SEDEX mineralization is associated with hydrothermal fluids of 100-300°C
- Microbial sulfate reduction is associated with temperatures of 0-80°C, whereas TSR is associated with temperatures of 100-350°C

Putting all these pieces of the puzzle together results in an evolutionary model in which the primary source of reduced sulfur in the depositional basin is microbial sulfate reduction until the hydrothermal vents arise and hot hydrothermal brines enter the system. These hot, dense brines hug the bottom of the depositional basin where their dissolved metals come in contact with the cold bottom waters. Initial mineralization of sulfide minerals occurs primarily with the sulfide that has been produced by microbes prior to the introduction of hydrothermal fluids into the local system, with perhaps some mixing from sulfide derived from a magmatic source.
As these hydrothermal vents become connected with the depositional basin, water from the system will be drawn down into the extensional faults in the underlying sediments and circulate there. The newly introduced water picks up more dissolved metals and increases in temperature as it moves through the fault network, turning it in hydrothermal fluid. This results in sufficient heating to reach temperatures above 100°C which causes TSR in these waters to reach geological significant reaction rates.
Once the initial, organically derived, sulfide species in the sub-basin is depleted, mineralization occurs with sulfide produced mostly by TSR that is introduced along with the hydrothermal brines. This mineralization takes place in a closed basin that causes an evolution of the isotopic composition of the sulfide and sulfate in the basin following the Rayleigh fractionation mechanism (Figure 20) that leads to isotopically heavy parent sulfate. This model is schematically shown in Figure 28.

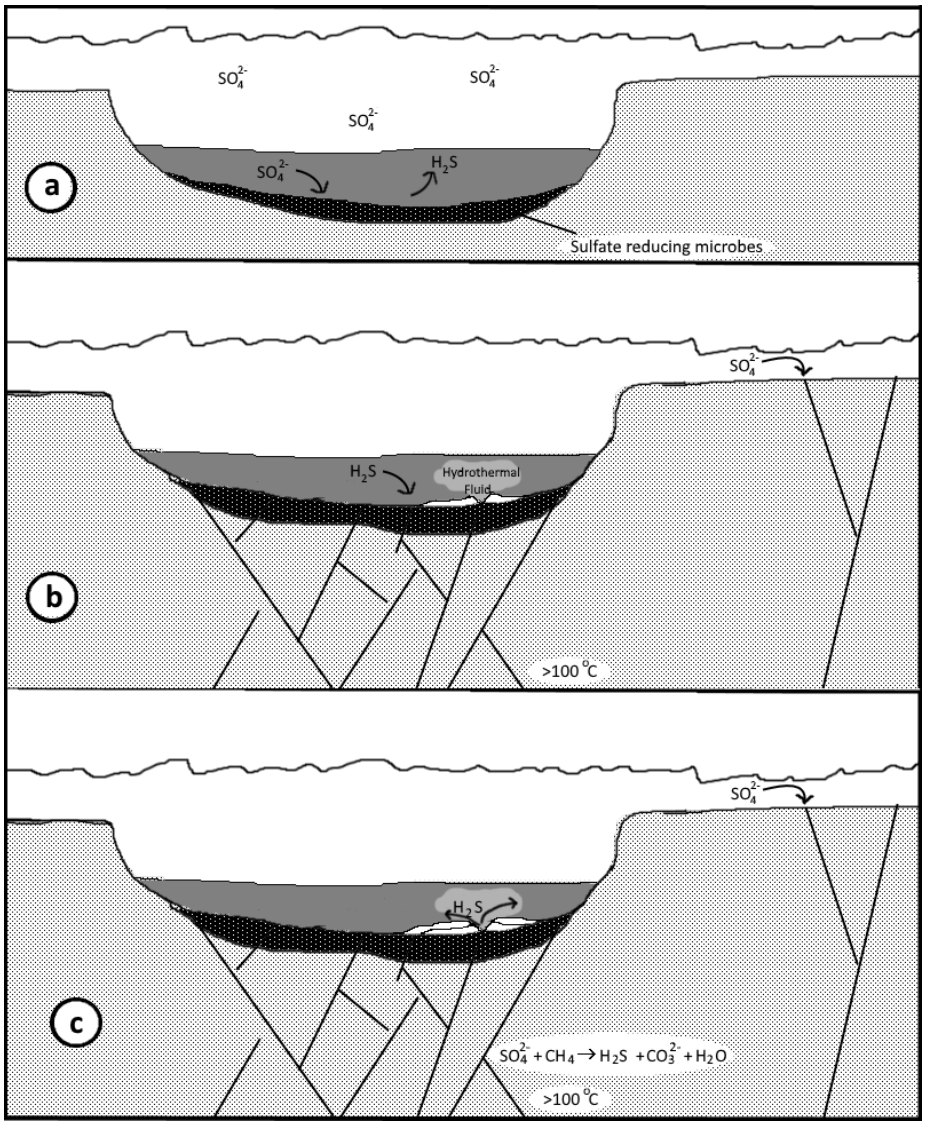

Figure 28: A schematic drawing of the genetic model for the change of microbial sulfate reduction to TSR as the primary source of reduced sulfur. **a:** Prior to the activation of the hydrothermal system at Gamsberg, H_2S was produced by reduction of sulfate derived from the seawater by micro-organisms present at the water-sediment interface. **b:** The hydrothermal system has reached Gamsberg and initial mineralization starts. The initial sulfide in the basin produced by microbial activity is used in this initial mineralization stage. Sulfate from the water column enters the hydrothermal system elsewhere and circulates through the fault network. **c:** The primary source of reduced sulfur has changed from microbial sulfate reduction to thermochemical reduction of sulfate derived from the seawater under high temperatures in the hydrothermal system.

6.2.3 Source of the initial sulfur

However, the significant increase of $\delta^{34}S$ values within the span of a few meters may be caused by other processes than a shift in the main source of reduced sulfur from microbial sulfate reduction to TSR. As mentioned before, the rate of precipitation of the sulfide minerals at the GVD038 locality is unknown and the $\delta^{34}S$ values observed at the top of unit B1 may be a positive anomaly. Taking these statements into consideration, the increase of $\delta^{34}S$ values through time may have been more gradual than what is observed in the stratigraphy. Therefore Rayleigh fractionation may have been more significant during the deposition of the Gamsberg deposit than is interpreted in this study.

Moreover, the initial source of sulfur is not known. Assumed before is that all the sulfur in the Gamsberg deposit is primarily derived from seawater, including the sulfide in the initial mineralization. It may however be possible that the sulfur in the initial hydrothermal brine was derived from magmatic H_2S, pore water or pre-existing sulfate minerals in the sediments. Sulfur of magmatic origin is associated with $\delta^{34}S$ values around 0‰ (Figure 17). Initial sulfide species derived from a magmatic source will be isotopically lighter and therefore show negative $\delta^{34}S$ values. Pre-existing sulfate- or sulfide minerals in the sediments may more closely reflect the isotopic composition of global seawater sulfate, or thereof derived sulfides, if these were deposited early enough in the history of the first order basin. More specifically, before the basin-wide Rayleigh fractionation that is interpreted form the compiled isotope data for the Aggeneys-Gamsberg district (Figure 21) occurred. Similarly pore water in the sediments may have retained a more primitive sulfur chemistry compared to the sulfate remaining in the seawater in the basin at the time the Gamsberg deposit formed. Any significant input of either magmatic derived sulfide, pore water sulfur or pre-existing sulfate- or sulfide minerals into the hydrothermal brine will increase the ^{32}S abundance in the sulfide mineralization and decrease the $\delta^{34}S$ signal observed.

6.2.4 Effects of metamorphism

Finally metamorphism could have influenced the the values and ranges of $\delta^{34}S$ that are reported in this study. Graphite is found in unit A3 and is indicative of high T metamorphism. In the B2-C2 units garnet and pyroxenoid, high grade metamorphic minerals, can be found in addition to garnet in unit A3. High temperatures associated with prograde metamorphism are known to alter the chemistry of the pyrrhotite-pyrite system. *Craig and Vokes, (1993)* described the changes in the pyrite-pyrrhotite system during a metamorphic cycle. If the pyrite-pyrrhotite system remains in equilibrium as temperature rises into the 300-600°C range during prograde heating, S_2 activity rises as pyrite releases sulfur and the pyrrhotite composition becomes more enriched in sulfur as the pyrite decomposes. This would be reflected by corroded pyrite grains and pyrite that is replaced by pyrrhotite. During retrograde cooling the activity of S_2 in the pyrite-pyrrhotite system decreases as a result of constant re-equilibration of the system. This results in the decrease of the sulfur content in pyrrhotite which allows for the growth of euhedral pyrite crystals (*Craig and Vokes, 1993*). Recrystallized pyrite can be recognized in thin section by annealed textures and

120° angles at grain boundary junctions.

Metamorphic textures such as 120° angles at grain boundary junctions, corrosion and overgrowths are observed in the samples form drillhole GVD038 from unit A3, where they are the most common, up to the B2 unit, where they are less common. Furthermore, graphite, a mineral associated with high temperature metamorphism was observed only in unit A3 by *Poignant-Molina (2017)* but not actively sought after. Other authors (*Stalder and Rozendaal, 2004; Foulkes, 2014*) report the presence of graphite as well in the B member of the Gams formation, namely in unit B1. *Stalder and Rozendaal, (2004)* explicitly mention unit B2 at Gamsberg to be graphite-free, but this has not been verified for drillhole GVD038.

Even though metamorphic textures were observed predominantly in the lower units of the succession, the presence of garnet and pyroxenoid in the upper B2-C2 units of the SEDEX units is an indication that the upper amphibolite facies metamorphism affected the top units as well, resulting in the formation of these secondary high-grade metamorphic minerals.

6.2.5 Mineralogical constraints of the redox state

Although pyrrhotite formation is associated with prograde metamophic heating of pyrite (*Craig and Vokes, 1993*), pyrrhotite can also form during metamorphism of iron mono-sulfide which is precipitated during the formation of sedimentary pyrite as a metastable intermediary species. FeS is formed initially when dissolved iron reacts with H_2S, and can subsequently react with H_2S to form pyrite (*Berner, 1984; Kao et al., 2004*). If the H_2S supply to intermediary iron sulfide species is insufficient, these metastable species may be preserved (*Kao et al., 2004*). In the upper units of the studied section pyrrhotite exists as the dominant iron sulfide mineral, found in large aggregates associated with sphalerite. Pyrite exists as a minor phase in these units, primarily found in the form of inclusions in pyrrhotite or in association with pyrrhotite. If the pyrrhotite in these units was formed out of pyrite during prograde metamorphism, it is expected that the retrograde phase of metamorphism would result in abundant pyrite in these units.

Furthermore previous authors (*Stalder and Rozendaal., 2004*) have mentioned the presence of an Apatite Marker Unit (AMU) located in between units B1 and B2 in the North orebody and the Overturned Limb. This unique unit was interpreted as a paleo-redox boundary by these authors as it marks a sharp boundary between the pyrite- and pyrrhotite-dominated units at these bodies. Although this unit bearing 10-20mm sized nodular apatite in a quartz-muscovite-sillimanite matrix is not found as a distinct layer in the studied section of drillhole GVD038, some similar features were observed in the studied units. Fine grained apatite nodules were reported in the B2 and C1 units as well as an increased abundance of muscovite and biotite in the B2 unit.

In addition to the change of a pyrite to a pyrrhotite dominated sulfide mineral assemblage and the presence of fine grained apatite nodules in the B2 and C1 units, which may be a lateral expression of the AMU observed at the North ore-

body and the Overturned Limb, minor manganese oxide phases were observed in the SQZ as well as abundant iron oxides in the C member. Furthermore the transition between the B and C units is marked by a decrease in sulfide minerals in favor of a gangue mineral assembly rich in Fe-oxides. All these mineralogical features combined reflect a change in the redox chemistry throughout drillhole GVD038 from anoxic conditions at the bottom of the section, sub-oxic conditions being reached in the SQZ and B2 units and becoming increasingly oxidized towards the top of the section. This is further backed up by the change of the dominant iron-oxide from magnetite to hematite upwards throughout the C2 unit, with iron becoming increasingly trivalent.

Nevertheless, the formation of iron sulfide and -oxide minerals at the same time during the deposition of the C member provides conflicting evidence on the redox state during deposition. The presence of both oxidized and reduced minerals alongside each other in the C member is therefore interpreted as the result of one of these mineral phases being secondary. Taking in account the interpretation of the B2 unit as sub-oxic and overlaying units as increasingly oxidized, it is likely that the sulfide minerals in the upper part of the stratigraphy are secondary features. This is further corroborated by the lack of metamorphic overgrowths and recrystallization observed in the sulfide minerals in the C member. Moreover, the sulfide mineral phases are predominantly found in grain boundaries between gangue minerals and micro-fractures in gangue minerals in the C member, especially in the C2 unit. In the C1 unit overall this effect is less pronounced due to the change in the mineral assemblage from abundant in sulfides and less abundant in gangue minerals to more abundant in gangue minerals at the expense of sulfides towards the C2 unit.

6.2.6 Metasomatic alteration

To explain the presence of secondary sulfide minerals in the oxic C member of drillhole GVD038 a mechanism is needed to transport the sulfide minerals. Metasomatism during metamorphism provides a mechanism that can not only transport the sulfide minerals from the anoxic and sub-oxic units of the Gams formation to the oxic C member, but also provides a medium for the transport of dissolved manganese needed to form the secondary Mn-bearing garnets and pyroxenoids to the C member. Before metamorphism took place the C member was likely void of both sulfides and major Mn-bearing phases. During peak metamorphism metasomatic fluid percolated through the sulfide- and Mn-rich units of the succession, dissolving some of the abundant Mn-rich sphalerite and iron sulfides, transporting them upwards through the succession and precipitating them in the C member. Some of the manganese was leached from this fluid and used in the formation of the pyroxenoid- and garnet minerals, resulting in the progressive depletion of manganese from sphalerite in these units.

6.3 Controls on the manganese content

This isotopic study has not found a one to one correlation between the Mn content of the sphalerites and the ore in general and the S isotopic signal. The study by *Poignant-Molina (2017)* on these samples revealed two interesting insights with respect to the manganese content. First and foremost a stable, high

manganese content around 6-7wt% up until unit C1 is reached, where manganese content drops down to around 1.5wt%. The second feature that is seen in these samples is the presence of the rare mineral alabandite (MnS) reported by *Poignant-Molina*. In the lower A3 unit, this mineral exceeds sphalerite in abundance. In unit B1, alabandite is still very much present as exsolutions in sphalerite grains. The SQZ unit contains finer grained exsolutions of alabandite in sphalerite grains as well as Mn-oxides. Alabandite was not reported in unit B2 by *Poignant-Molina*, and this is where Mn concentrations in the sphalerites begin to drop.
As mentioned before, the sphalerite crystal structure can only accommodate up to ±6-7wt% MnS before this exsolves into separate alabandite grains. Taking this into account, one can link the decline in the sphaleritic Mn content starting at the boundary of units B2 and C1 to the pattern of decreasing alabandite grain sizes as we go up the stratigraphy until they disappear in unit B2.

In the SQZ unit, however, manganese was reported in minor oxide phases tentatively interpreted as pyrolusite (MnO_2) by *Poignant-Molina (2017)*, indicating a tetravalent manganese species. Manganese is found as a divalent species in the C member in gangue mineral phases, including spessartine or calderite and rhodonite, which become increasingly dominant in the mineral assemblage over the span of the C1 unit.
In the B1 unit, however no non-sulfide minerals in which manganese exists as a divalent species were observed. In the A3 unit manganese was encountered in several manganiferous carbonate phases including rhodochrosite and manganoan calcite. Garnet and pyroxenoid were reported in the A3 unit as well but in contrast to the garnet and pyroxenoid in the B2-C2 units are not Mn-bearing minerals.

The mineral assemblage throughout the stratigraphy reflects two manganese signals. First, manganese in sulfide phases is mainly contained within alabandite and sphalerite. Some Mn may be found as a trace element in pyrrhotite but in significantly smaller concentrations. As discussed above the grain size and abundance of alabandite decreases upwards in the stratigraphy. Manganese inside the sphalerite crystal structure stays relatively constant at the upper limit of accommodation around ±6-7wt% MnS until unit B2 where no more alabandite grains are found inside sphalerite and manganese content in sphalerite grains begins to fall.
Secondly, in the gangue mineral phases manganese is initially dominant in carbonate phases. Going upward in the stratigraphy manganese-bearing gangue minerals are not observed in unit B1, whilst alabandite grain sizes decrease throughout this layer. In the SQZ unit manganese in gangue minerals is encountered in the form of minor oxide phases that were tentatively interpreted as (MnO_2). These oxide phases may however be MnO instead, which is more in line with a more discrete increase towards more oxidized conditions during deposition. In unit B2 gangue minerals are dominated by quartz and garnet, the latter of which may contain manganese as a divalent species. Going up towards the top of the studied section manganese-bearing garnet and pyroxenoid phases as well as other gangue minerals become more abundant in the mineral assemblage at the expense of sulfide minerals.

6.3.1 A model for the Mn abundance throughout drillhole GVD038

By combining the manganese signals in the sulfide- and gangue minerals the evolution of the Mn abundance throughout the stratigraphy of drillhole GVD038 can be assessed. Proposed is a model in which manganese from a finite source was incorporated with the sphalerite mineralization as well as in gangue minerals. When mineralization of the Gamsberg deposit started, the initial hydrothermal brine became very enriched in manganese relative to other base metals. This dissolved manganese was deposited as alabandite in association with sphalerite or as distinct alabandite grains as well as in carbonate phases. In the case that the alabandite minerals are associated with sphalerite, this is a likely result of the sphalerite mineral structure not being able to accommodate such large quantities of manganese and exsolving most of it as alabandite. Later textural re-equilibration observed by *Poignant-Molina (2017)* may have contributed to the formation of large continuous alabandite grains in this scenario. As mineralization continued the originally manganese enriched hydrothermal fluids became less and less enriched in manganese, causing alabandite to exist only as exsolutions from sphalerite and the abundance and size of these alabandite exsolutions to decrease, resulting in the progressively smaller alabandite grains being localized within the larger sphalerite grains observed in the B1 and SQZ units. In addition, the originally manganese enriched hydrothermal fluids becoming less and less enriched in manganese also resulted in the absence of manganese-bearing gangue minerals in unit B1. In the SQZ unit the redox conditions were more oxidized and some manganese was precipitated in minor oxide phases. The process of continuous depletion of manganese in the hydrothermal brine and resulting smaller exsolved alabandite grains continued up until unit B2, in which exsolution is no longer confidently observed at the micro scale and gangue minerals which may contain manganese as a divalent species become more prevalent. At this point during the deposition the manganese content in the hydrothermal brine could be fully accommodated by the sphalerite mineral grains. From unit C1 upward, incorporation of manganese in garnet and pyroxenoid became increasingly prevalent. Together with the manganese depletion of the initial hydrothermal fluid, which resulted in the progressively decreasing size of the alabandite grains and exsolutions during initial mineralization, the manganese distribution throughout the section was controlled by the secondary redistribution of sulfide minerals into the oxic C1 and C2 units by metasomatism, which was accompanied by incorporation of manganese in gangue minerals in favor of sphalerite, resulted in the depletion of manganese in the secondary sphalerite geochemistry until levels around 1.5wt% Mn in sphalerite were reached.

6.3.2 The source of manganese

One key element that has not been discussed yet is the source of the manganese enrichment in the Gamsberg deposit. Based on the sulfur isotope data and the manganese concentrations produced by *Poignant-Molina (2017)* it was argued above that manganese was most prevalent at the bottom of the Gams formation and progressively depleted as the deposit grew and the local chemistry evolved. A second aspect that was discussed before that gives a clue about the

development of the Gamsberg deposit is the increase in $\delta^{34}S$ values from west to east in the Aggeneys-Gamsberg deposit, culminating in the highest values found at Gamsberg. This indicates that in the scope of a closed primary basin, the Gamsberg deposit formed later than the Aggeneys deposits. These combined factors allow for a spatial and temporal framework in which the Aggeneys deposits affect the chemistry of the Gamsberg deposit.

A feature of SEDEX mineralization is the distribution and zonation of the various base metals in these deposits. Manganese, along with Fe and PO_4 is often found as an enrichment in shales distal with respect to the hydrothermal vent (*Emsbo, 2009*). The stability of MnS is very limited in natural environments and Mn usually exists in reduced environments as a dissolved species or other minor phases (Figure 15). Proposed is a model in which Mn, in the form of Mn^{2+} and Fe-Mn-silicates, exhaled by the hydrothermal vents that formed the Aggeneys SEDEX deposits are transported by density driven flow to the topographical depression where the Gamsberg deposit would later be formed. These Mn species precipitated in the organic shales and carbonates in the area and thusly enriched the sediments. When a hydrothermal system surfaced at Gamsberg, the hot metalliferous brines remobilized the manganese in the sediments and carbonates, allowing the manganese to be precipitated along with the sulfide minerals. This initial manganese source was finite however, as most of the SEDEX mineralization in the Aggeneys district ceased, no new residual Mn flux towards the Gamsberg locality existed, making the deeper sediments from which the other base metals are derived an increasingly important manganese source as the manganese input from the initially enriched sediments decreased.

6.4 Synthesis

Now that the observed $\delta^{34}S$ values, Mn concentrations, mineral assemblage variations and metamorphic features throughout the stratigraphy of drillhole GVD038 as well as the source of the manganese enrichment in these rocks have been assessed, it is possible to construct a dynamic genetic model that integrates all these interpretations and explains why the Gamsberg zinc deposit is so enriched in manganese and why the rare MnS mineral alabandite is so prevalent in this deposit:

The Aggeneys-Gamsberg deposits were formed in the same, closed-system first-order extensional basin which contained multiple second- and third-order sub-basins. In the west of the Aggeneys district hydrothermal systems surface and SEDEX mineralization started at Swartberg, and subsequently at Broken Hill and Big Syncline. The formation of these deposits was associated with significant thermochemical sulfate reduction (TSR) from seawater derived sulfate in the hydrothermal systems as well as microbial sulfate reduction at the water-sediment interface. These mechanisms of sulfate reduction progressively depleted the dissolved sulfate species in the basin of the light sulfur isotope, ^{32}S which caused a progressive ^{34}S enrichment of the remaining dissolved sulfate. Besides an enrichment in sulfide and ^{34}S, the formation of these deposits also introduced significant quantities of exhaled Mn in the basin which accumulated as carbonates and Fe-Mn silicates in organics-rich sediments in the third order basin which would later host the Gamsberg deposit.

When the extensional fault framework in the basin reached Gamsberg, the hydrothermal system became connected with this locality as well. Hot brines formed under the Gamsberg locality and moved upwards taking up base metals in the deeper sediments. Further up in the sedimentary cover these hot metalliferous brines mobilized the residual manganese species and took these to the basin surface. Here the hot brines came in contact with the cold, H_2S-rich, bottom waters, immediately decreasing the solubility of the dissolved metals in the brine and precipitated them as sulfide. As alabandite is more stable at slightly alkaline conditions (Figure 15) it can be deduced from the metal-sulfide precipitation diagram (Figure 29) that activity of $Zn^{2+} < Fe^{2+} < Mn^{2+}$ and that precipitation occurred in this order.

The initial H_2S was either formed by microbial sulfate reduction which resulted in isotopically very light sulfide when accounted for the isotopically very heavy seawater sulfate from which it was derived, or derived thermochemically from sulfur from a magmatic source, more primitive sulfate present in pore waters or sulfide minerals with a more primitive isotopic composition present in the sediment. This initial H_2S became depleted by this sudden draw-down into sulfide minerals and was not replenished at significant rates. Sulfate from the seawater that entered the hydrothermal system elsewhere in the fault network got reduced by TSR, under high temperatures in the order of 120-300°C. These new hydrothermal fluids circulated throughout the sediments under the Gamsberg deposit, taking up the base metals from the deep sediments and additional Mn from the top sediments before resurfacing and precipitating minerals with predominantly TSR derived sulfide.

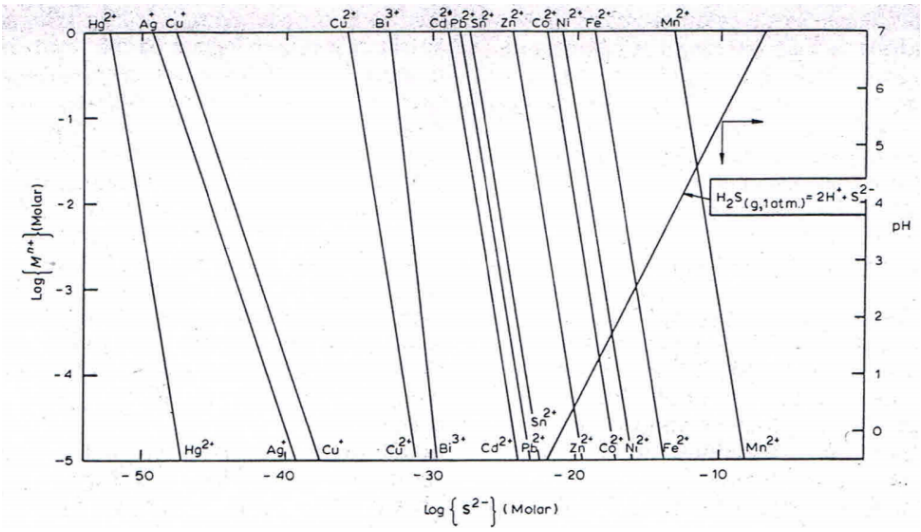

Figure 29: A precipitation diagram for metal-sulfide minerals as a function of pH and sulfide activity at 1amt and 25°C. Sulfide activity is determined from this graph using the pH of the solution plotted at the right axis. The activity of the metal ions shown at the left axis is then read from this graph using the corresponding sulfide activity at the bottom axis. (From Monhemius (1977))

.

The first few meters of mineralization were very enriched in manganese, allowing even alabandite to precipitate as discrete grains, perhaps catalyzed by the presence of sphalerite. As mineralization at Gamsberg continued the initially manganese enriched sediments became increasingly depleted in manganese, which is reflected in the rocks from drillhole GVD038. Alabandite minerals became much smaller in size and changed from distinct grains to exsolutions in larger sphalerite grains. The grain sizes of the alabandite exsolutions in the sphalerites decreased until the manganese content in the rocks had decreased to levels which can be fully accommodated by the sphalerite mineral structure, and no distinct alabandite phases could be observed anymore.
Around the time of deposition of the SQZ and B2 units, a chemocline in the basin was reached and the redox state changed from anoxic to sub-oxic, becoming increasingly oxidized. Primary iron sulfide mineralization in the B2 unit is dominated by FeS that did not mature into pyrite due to insufficient H_2S being available as sphalerite mineralized before FeS due to Zn^{2+} reacting with H_2S before Fe^{2+} (Figure 29). Units C1 and C2 were deposited initially without sulfide minerals but rather with abundant iron oxides and other gangue minerals, after which primary mineralization ceased.

During the Kibaran- (1.21-1.17Ga) and primarily the Namaquan orogeny (1.06-1.03Ga) the succession was heavily metamorphosed, reaching upper amphibolite facies in the peak metamorphic M_2 phase. As a result of metamorphism garnets and pyroxenoids were formed, pyrite reacted to form pyrrhotite and FeS was turned into pyrrhotite. Along with the metamorphism, metasomatism occurred. Metasomatic fluids percolated through the succession, dissolved some of the iron sulfides and sphalerite and transported these to the oxic C1 and C2 units where these precipitated. The manganese dissolved in these metasomatic fluids was under influence of the high grade metamorphic conditions incorporated in the newly formed garnets and pyroxenoids rather than in the sphalerite, causing the manganese content in secondary sphalerite to drop.

7 Summary and conclusions

LA-ICP-MS analyses of 34 samples from drillhole GVD038 from the Gamsberg zinc deposit, Namaqualand Metamorphic Province, Northern Cape Province, South Africa resulted in two sets of $\delta^{34}S$ sulfur isotope data that capture the variability of the sulfur isotopic composition of the Gams formation throughout the vertical stratigraphy. These analyses both revealed a first order pattern in which the older A3 and B1 unit show isotopic fractionations of -43 to -23‰ relative to VCDT compared to the isotopic composition of sulfate minerals (barite) observed at this locality, ±33‰. These low values are attributed to either microbial reduction of sulfate derived from seawater, or sulfur derived from within the sediments being the primary source of reduced sulfur in the system at this point in the depositional history. During the deposition of unit B1 the isotopic composition became considerably heavier in a very short timeframe, with $\delta^{34}S$ values reaching, and remaining fairly stable at +7‰ in the Fe-sulfides and -3‰ in the sphalerites compared to the barite. These values are attributed to fractionation by means of thermochemical sulfate reduction (TSR) under high temperatures, although the isotopic composition of the Fe-sulfides remained very

heavy. This was interpreted as a result of prograde and subsequent retrograde metamorphism of the pyrite-pyrrhotite system.

Furthermore the data on Mn variability in these same 34 samples from *Poignant-Molina (2017)*, in combination with the detailed petrographic description of the samples in that study was reassessed and a different interpretation was made. Alabandite minerals are interpreted as features that show that the upper limit of accommodation of MnS in the sphalerite mineral structure was exceeded, which is supported by the maximum Mn content of the sphalerite minerals studied by *Poignant-Molina (2017)* to lay around 6.5wt%: the upper limit of MnS accommodation the sphalerite mineral structure allows for before exsolution of alabandite occurs. Once alabandite minerals are no longer observed in the stratigraphy the Mn content in the sphalerite grains starts to decline from 6.5wt%. The maximum abundance of Mn minerals can be found in the bottom most unit of the Gams formation at this locality, progressively decreasing going up in the stratigraphy. This was interpreted as the result of an initial enrichment of Mn in the shallow sediments at the Gamsberg locality as a distal expression of the formation of the older Aggeneys SEDEX deposits. Manganese from these older hydrothermal vents did not get mineralized locally and was deposited in the organics rich sediments at the Gamsberg locality, where it was remobilized when hydrothermal activity started there.

The redox-state of the succession was interpreted to have shifted from anoxic in the bottom units, where pyrite and other sulfide minerals are abundant, to sub-oxic in the SQZ unit and primarily the B2, unit where the dominant Fe-sulfide mineral changed from Pyrite to FeS which was later metamorphosed into pyrrhotite, becoming increasingly oxidized further upwards. Metasomatism during peak metamorphism was interpreted as the source of secondary sulfide minerals in the top C1 and C2 units which are characterized by abundant primary Fe-oxides, as well as the mechanism that transported manganese to these top units where it was incorporated in secondary garnet and pyroxenoid under the high-grade metamorphic conditions rather than in sphalerite, which became increasingly depleted as the abundance of these metamorphic minerals increased.

7.1 Recommendations for future work

Although this study and the previous study by *Poignant-Molina (2017)*, provided some very interesting insights and constraints for the genesis of the Gamsberg Zinc Deposit, in combination with the study of *Foulkes (2014)* who provided additional basin-wide geochemical constraints for the Aggeneys-Gamsberg district, further study of these rocks is needed to verify some of the hypotheses and assumptions on which models made in this study are based.

First of all, a full geochemical assessment of either the bulk rock composition or the bulk sulfides composition throughout the stratigraphy of drillhole GVD038 should provide the necessary Mn variability throughout this sequence. In this study the upper limit of MnS accommodation in the sphalerite mineral structure and the presence of alabandite exsolutions and distinct alabandite grains in the parts of the stratigraphy where this upper limit was reached, were combined and

interpreted as manganese being an initially enriched, but progressively depleting component. Bulk rock chemistry should be assessed to verify this hypothesis.

Secondly the Mn- and δ^{34}S variability throughout the stratigraphy of the Gams formation should be studied in the other Gamsberg orebodies as well. Whilst the models provided here account for the variability of δ^{34}S and Mn throughout the stratigraphy of drillhole GVD038 and to a larger extent to part of the western orebody, no new definite constraints can be made for the genesis of the Northern-, Southern- and Eastern orebodies, as well as the Overturned Limb. The Mn variability study of drillhole GAM107 in the North orebody, carried out by geologists commissioned by Vedanta, can be expanded upon by a stable sulfur isotope study on the sulfide minerals in drillhole GAM107 similar to the one in this study. The stable isotope study on the North orebody carried out by *Foulkes (2014)* (drillhole G1) does already provide some constraints for the North orebody, but lateral variations between the GAM107 and G1 drillholes may influence any comparison drawn between these two studies.

Thirdly a differentiation may be made between microbially reduced sulfur derived from dissolved sulfate in the sub-basin or reduced sulfur derived from magmatic sources or primitive sulfate and sulfides in the sediments as the primary source of the initial sulfide that mineralized in the lower B1 and A3 units. This can be quantified by mass balance mixing models.

Furthermore the formation of the alabandite grains from drillhole GVD038 should be studied in more detail. It is still unknown if the discrete alabandite grains found in unit A3 were formed as separate grains or if these are associated with sphalerite mineralization, similarly to the exsolved alabandite species. A study on the sulfur isotope variability of different alabandite species throughout the stratigraphy can reveal if the sulfur isotope ratio in the discrete alabandite grains differs significantly from the sulfur isotope ratio found in the exsolved alabandite grains found in the sphalerite grains. The exsolved alabandite species is likely to show a strong isotopic control by the chemistry of the surrounding sphalerite grain.

In addition, the isotopic variability of the parent sulfate through time is poorly constrained at Gamsberg. Whilst the massive barite found at Gamsberg is assumed to reflect the parent sulfate, based on the interpretation by previous authors that the barite and sulfide deposits are stratigraphically equivalent (*McClung et al., (2007)*), the sulfur isotope variability of this barite deposit is poorly constrained. Both *McClung et al., (2007)* and *von Gehlen, (1983)* analyzed only two barite samples each and did not record their absolute stratigraphic depths. A study on the sulfur isotope variability throughout the barite deposit at Gamsberg could provide insights in the rate of Rayleigh fractionation which can be correlated against the increase in δ^{34}S values at the bottom of The B unit from drillhole GVD038, although it may be difficult to determine the exact depths of the stratigraphic equivalents of the sulfide-rich units A, B and C in the massive barite.

Finally, the interpretation made by *Poignant-Molina (2017)*, who argued that the depletion of manganese in the upper units of the Gams formation only is

a result of the uptake of manganese and iron as divalent or trivalent species in other mineral phases, may still be valid. Although the results of *Poignant-Molina (2017)* were interpreted differently in this study, with an additional finite initial manganese enrichment being present in the sediments that was subsequently depleted during deposition accessory to the speciation of divalent manganese in other minerals due to metasomatism, both interpretations remain viable until they are either verified or falsified. Future research on the geochemical composition of the other minerals which may take up Fe and Mn as di- or trivalent species, such as Fe-Mn silicates, carbonates and oxides; throughout the stratigraphy of drillhole GVD038 is needed to settle this matter.

8 Acknowledgements

I would like to thank the people who helped complete this thesis.
First of all my supervisors Paul Mason and Harilaos Tsikos who pitched this intriguing project to me and provided constructive criticism and helpful insights along the way.
I would also like to thank Helen de Waard who has assisted me with the ICP-MS analyses and helped to tremendously improve the methodology of these analyses.
A special thanks goes out to Léo Poignant-Molina who did not only provide an extraordinary petrographic description and geochemical analysis of these samples, but also provided me his raw data which helped to improve the dataset I produced.
I would also like to thank the Petrology Group of the Earth Sciences Department at Utrecht University for their critical questions and remarks which helped me to put the last pieces of the puzzle in place.
Thank you to my sister Linda, for giving me some tips to make lab-life a lot easier.

Finally I would like to thank my friends Sander, Mahid, Marina and Estefania, who provided the perfect excuse to take brakes during analysis sessions and helped me from going insane from that repetitive process.

9 References

Abraitis, P. K., Pattrick, R. A. D., & Vaughan, D. J. (2004). Variations in the compositional, textural and electrical properties of natural pyrite: a review. International Journal of Mineral Processing, 74(1-4), 41-59.

Anderson, G. M., & Thom, J. (2008). The role of thermochemical sulfate reduction in the origin of Mississippi Valley-type deposits. II. Carbonate–sulfide relationships. Geofluids, 8(1), 27-34.

Arnold, R. G. (1967). Range in composition and structure of 82 natural terrestrial pyrrhotites. The Canadian Mineralogist, 9(1), 31-50.

Ayuso, R. A., Kelley, K. D., Leach, D. L., Young, L. E., Slack, J. F., Wandless, J. F., ... & Dillingham, J. L. (2004). Origin of the red dog Zn-Pb-Ag deposits, Brooks Range, Alaska: evidence from regional Pb and Sr isotope sources. Economic Geology, 99(7), 1533-1553.

Bailie, R., Armstrong, R., & Reid, D. (2007a). The Bushmanland Group supracrustal succession, Aggeneys, Bushmanland, South Africa: provenance, age of deposition and metamorphism. South African Journal of Geology, 110(1), 59-86.

Bailie, R., Armstrong, R., & Reid, D. (2007b). Composition and single zircon U-Pb emplacement and metamorphic ages of the Aggeneys Granite Suite, Bushmanland, South Africa. South African Journal of Geology, 110(1), 87-110.

Berner, R. A. (1984). Sedimentary pyrite formation: an update. Geochimica et cosmochimica Acta, 48(4), 605-615.

Canfield, D. E. (2004). The evolution of the Earth surface sulfur reservoir. American Journal of Science, 304(10), 839-861.

Canfield, D. E. (2005). The early history of atmospheric oxygen: homage to Robert M. Garrels. Annu. Rev. Earth Planet. Sci., 33, 1-36.

Canfield, D. E., & Farquhar, J. (2009). Animal evolution, bioturbation, and the sulfate concentration of the oceans. Proceedings of the National Academy of Sciences, 106(20), 8123-8127.

Canfield, D. E., & Thamdrup, B. (1994). The production of 34S-depleted sulfide during bacterial disproportionation of elemental sulfur. Science, 266(5193), 1973-1975.

Chambers, L. A., & Trudinger, P. A. (1979). Microbiological fractionation of stable sulfur isotopes: a review and critique. Geomicrobiology Journal, 1(3), 249-293.

Cook, N. J., Ciobanu, C. L., Pring, A., Skinner, W., Shimizu, M., Danyushevsky, L., ... & Melcher, F. (2009). Trace and minor elements in sphalerite: A LA-ICPMS study. Geochimica et Cosmochimica Acta, 73(16), 4761-4791.

Cornell, D. H., Thomas, R. J., Gibson, R., Moen, H. F. G., Reid, D. L., Moore, J. M., & Gibson, R. L. (2006). The Namaqua-Natal Province. Geological Society of South Africa.

Cornell, D. H., Pettersson, A., Whitehouse, M. J., & Scherstén, A. (2009). A new chronostratigraphic paradigm for the age and tectonic history of the Mesoproterozoic Bushmanland ore district, South Africa. Economic Geology, 104(3), 385-404.

Craig, J. R. & Vokes, F. M. (1993). The metamorphism of pyrite and pyritic ores: an overview. Mineral. Mag, 57, 3-18.

Davidson, G. J. (1998). Alkali alteration styles and mechanisms, and their implications for a 'brine factory'source of base metals in the rift-related McArthur group, Australia. Australian Journal of Earth Sciences, 45(1), 33-49.

Deer, W. A., Howie, R. A., & Zussman, J. (1962). Rock-forming Minerals: Vol. 5: Non-silicates. Longman.

Dewey, J. F., Robb, L., & Van Schalkwyk, L. (2006). Did Bushmanland extensionally unroof Namaqualand?. Precambrian Research, 150(3-4), 173-182.

Eldridge, C. S., Williams, N., & Walshe, J. L. (1993). Sulfur isotope variability in sediment-hosted massive sulfide deposits as determined using the ion microprobe SHRIMP; II, A study of the HYC Deposit at McArthur River, Northern Territory, Australia. Economic Geology, 88(1), 1-26.

Emsbo, P., & Johnson, C. A. (2004). Formation of modern and Paleozoic stratiform barite at cold methane seeps on. Geology, 32, e64.

Emsbo, P. (2009). Geologic criteria for the assessment of sedimentary exhalative (sedex) Zn-Pb-Ag deposits. US Geological Survey Open-File Report, 1209, 21.

Emsbo, P., Seal, R. R., Breit, G. N., Diehl, S. F., & Shah, A. K. (2016). Sedimentary exhalative (sedex) zinc-lead-silver deposit model (No. 2010-5070-N). US Geological Survey.

Foulkes, S. E. (2014). New Geochemical Constraints on the Genesis of the Gamsberg Zinc Deposit, Namaqualand Metamorphic Province, South Africa (Doctoral dissertation, Rhodes University).

Fu, J., Hu, Z., Zhang, W., Yang, L., Liu, Y., Li, M., ... & Hu, S. (2016). In situ sulfur isotopes (δ^{34}S and δ^{33}S) analyses in sulfides and elemental sulfur using high sensitivity cones combined with the addition of nitrogen by laser ablation MC-ICP-MS. Analytica chimica acta, 911, 14-26.

Gardner, H. D., & Hutcheon, I. (1985). Geochemistry, mineralogy, and geology of the Jason Pb-Zn deposits, Macmillan Pass, Yukon, Canada. Economic Geology, 80(5), 1257-1276.

Goodfellow, W. D. (2007). Mineral deposits of Canada: A synthesis of major deposit-types, district metallogeny, the evolution of geological provinces, and exploration methods (No. 5). Geological Association of Canada, Mineral Deposits Division.

Graham, J. (1978) Manganochromite, palladium antimonide, and some unusual mineral associations at the Nairne pyrite deposit, South Australia. American Mineralogist, 63, 1166-1174

Habicht, K. S., & Canfield, D. E. (1997). Sulfur isotope fractionation during bacterial sulfate reduction in organic-rich sediments. Geochimica et Cosmochimica Acta, 61(24), 5351-5361.

Habicht, K. S., Gade, M., Thamdrup, B., Berg, P., & Canfield, D. E. (2002). Calibration of sulfate levels in the Archean ocean. Science, 298(5602), 2372-2374.

Harrison, A. G., & Thode, H. G. (1958). Mechanism of the bacterial reduction of sulphate from isotope fractionation studies. Transactions of the Faraday Society, 54, 84-92.

Hewett, D. F., & Rove, O. N. (1930). Occurrence and relations of alabandite. Economic Geology, 25(1), 36-56.

Hoffmann, D. (1994). Geochemistry and genesis of manganiferous silicate-rich iron formation bands in the Broken Hill deposit, Aggeneys, South Africa. Exploration and Mining Geology, 3, 407-417.

Horita, J., Zimmermann, H., & Holland, H. D. (2002). Chemical evolution of seawater during the Phanerozoic: Implications from the record of marine evaporites. Geochimica et Cosmochimica Acta, 66(21), 3733-3756.

Hunt, J. M. (1996). Petroleum geochemistry and geology (Vol. 2, pp. 1-743). New York: WH Freeman.

Hurai, V., & Huraiová, M. (2011). Origin of ferroan alabandite and manganoan sphalerite from the Tisovec skarn, Slovakia. Neues Jahrbuch für Mineralogie-Abhandlungen: Journal of Mineralogy and Geochemistry, 188(2), 119-134.

Joubert, P. (1971) The regional tectonism of the gneisses of part of the Namaqualand. Bulletin of the Precambrian Research Unit, University of Cape Town, 10, p. 220.

Kah, L. C., Lyons, T. W., & Frank, T. D. (2004). Low marine sulphate and protracted oxygenation of the Proterozoic biosphere. Nature, 431(7010), 834.

Kao, S. J., Horng, C. S., Roberts, A. P., & Liu, K. K. (2004). Carbon–sulfur–iron relationships in sedimentary rocks from southwestern Taiwan: influence of geochemical environment on greigite and pyrrhotite formation. Chemical Geology, 203(1-2), 153-168.

Kharaka, Y. K., Maest, A. S., Carothers, W. W., Law, L. M., Lamothe, P. J., & Fries, T. L. (1987). Geochemistry of metal-rich brines from central Mississippi salt dome basin, USA. Applied Geochemistry, 2(5-6), 543-561.

Krouse, H. R., & Coplen, T. B. (1997). Reporting of relative sulfur isotope-ratio data (technical report). Pure and Applied Chemistry, 69(2), 293-296.

Large, R. R., Bodon, S. B., & Davidson, G. J. (1996). The chemistry of BHY ore formation-one of the keys to understanding the differences between SEDEX and BHT deposits. In New Developments in Broken Hill Type Deposits (Vol. 1, pp. 105-112).

Large, R. R., Bull, S. W., Selley, D., Yang, J., Cooke, D., Garven, G., & McGoldrick, P. (2002). Controls on the formation of giant stratiform sediment-hosted Zn-Pb-Ag deposits: with particular reference to the north Australian Proterozoic. University of Tasmania, Centre for Ore Deposit Research Special Publication, 4, 107-149.

Leach, D. L., Marsh, E., Emsbo, P., Rombach, C. S., Kelley, K. D., & Anthony, M. (2004). Nature of hydrothermal fluids at the shale-hosted red dog Zn-Pb-Ag deposits, Brooks Range, Alaska. Economic Geology, 99(7), 1449-1480.

Leach, D. L., Sangster, D. F., Kelley, K. D., Ross, R. L., Garven, G., & Allen, C. R. (2005). Sediment-hosted Pb-Zn deposits: a global perspective. Economic Geology, 100, 561-608.

Lyons, T. W., Gellatly, A. M., McGoldrick, P. J., & Kah, L. C. (2006). Proterozoic sedimentary exhalative (SEDEX) deposits and links to evolving global ocean chemistry. MEMOIRS-GEOLOGICAL SOCIETY OF AMERICA, 198, 169.

Machel, H. G., Krouse, H. R., & Sassen, R. (1995). Products and distinguishing criteria of bacterial and thermochemical sulfate reduction. Applied geochemistry, 10(4), 373-389.

Machel, H. G. (2001). Bacterial and thermochemical sulfate reduction in diagenetic settings—old and new insights. Sedimentary Geology, 140(1-2), 143-175.

Mason, P. R., Košler, J., de Hoog, J. C., Sylvester, P. J., & Meffan-Main, S. (2006). In situ determination of sulfur isotopes in sulfur-rich materials by laser ablation multiple-collector inductively coupled plasma mass spectrometry (LA-MC-ICP-MS). Journal of Analytical Atomic Spectrometry, 21(2), 177-186.

McClung, C.R. (2006). Basin analysis of the Bushmanland Basin, Namaqualand Metamorphic Complex, Northern Cape Province, South Africa. Unpublished PhD thesis, University of Johannesburg, South Africa.

McClung, C.R., Gutzmer, J., Beukes, N.J., Mezger, K., Strauss, H., Gertloff, E. (2007) Geochemistry of bedded barite of the Mesoproterozoic Aggeneys-Gamsberg Broken Hill-type district, South Africa. Mineralium Deposita, 42 (5), pp. 537-549.

McClung, C.R., Gutzmer, J., Gertloff, E., Beukes, N. And Strauss, H. (2010). Sulfur isotopes of base-metal sulfide and barite pairs from the Aggeneys-Gamsberg BHT district, South Africa. Geological Society of America Abstract with Programs, 42 (5), 579.

McClung, C.R., Viljoen, F. (2011) A detailed mineralogical assessment of sphalerites from the Gamsberg zinc deposit, South Africa: The manganese conundrum. Minerals Engineering, 24 (8), pp. 930-938.

Monhemius, A. J. (1977). Precipitation diagrams for metal-hydroxides, sulfides, arsenates and phosphates. Transactions of the institution of mining and metallurgy section c-mineral processing and extractive metallurgy, 86(DEC), C202-C206.

Moses, A.M. (2015) The deportment of manganese of the Gasmberg East orebody, South Africa. MSc thesis *(unpublished)*, University of Pretoria, p. 193.

Mücke, A., Dzigbodi-Adjimah, K., & Annor, A. (1999). Mineralogy, petrography, geochemistry and genesis of the Paleoproterozoic Birimian manganese-formation of Nsuta/Ghana. Mineralium Deposita, 34(3), 297-311.

Olivo, G. R., & Gibbs, K. (2003). Paragenesis and mineral chemistry of alabandite (MnS) from the Ag-rich Santo Toribio epithermal deposit, Northern Peru. Mineralogical Magazine, 67(1), 95-102.

Parr, J. M., & Plimer, I. R. (1995). Models for Broken Hill-type lead-zinc-silver deposits. Geological Association of Canada.

Poignant-Molina, L (2017). Primary controls on iron and manganese distribution in sphalerite of the Gams Formation, Gamsberg Zinc Deposit, Namaqualand, South Africa. Unpublished MSc Thesis, Rhodes University, South Africa.

Rees, C. E. (1973). A steady-state model for sulphur isotope fractionation in bacterial reduction processes. Geochimica et Cosmochimica Acta, 37(5), 1141-1162.

Reid, D.L., Welke, H.J., Erlank, A.J., Betton, P.J. (1987) Composition, age and tectonic setting of amphibolites in the central Bushmanland Group, Western Namaqua Province, southern Africa. Precambrian Research, 36 (2), pp. 99-126.

Reid, D. L., Smith, C. B., Watkeys, M. K., Welke, H. J., & Betton, P. J. (1997). Whole-rock radiometric age patterns in the Aggeneys-Gamsberg ore district, central Bushmanland, South Africa. South African Journal of Geology, 100(1), 11-22.

Rickard, D., & Luther, G. W. (2007). Chemistry of iron sulfides. Chemical reviews, 107(2), 514-562.

Robb, L. J., Armstrong, R. A., & Waters, D. J. (1999). The history of granulite-facies metamorphism and crustal growth from single zircon U–Pb geochronology: Namaqualand, South Africa. Journal of Petrology, 40(12), 1747-1770.

Rodushkin, I., Pallavicini, N., Engström, E., Sörlin, D., Öhlander, B., Ingri, J., & Baxter, D. C. (2016). Assessment of the natural variability of B, Cd, Cu, Fe, Pb, Sr, Tl and Zn concentrations and isotopic compositions in leaves, needles and mushrooms using single sample digestion and two-column matrix separation. Journal of Analytical Atomic Spectrometry, 31(1), 220-233.

Rozendaal, A. (1975). The geology of Gamsberg, Namaqualand, South Africa. *Unpublished MSc thesis*, University of Stellenbosch, Stellenbosch, South Africa. 109pp.

Rozendaal, A. (1986) The Gamsberg Zinc Deposit, Namaqualand District. In: Anhaeusser, C.R. and Maske, S. (Eds.) Mineral Deposits of Southern Africa (1986), 1477-1488. Geological Society of South Africa.

Schindelin, J., Arganda-Carreras, I., Frise, E., Kaynig, V., Longair, M., Pietzsch, T., ... & Tinevez, J. Y. (2012). Fiji: an open-source platform for biological-image analysis. Nature methods, 9(7), 676.

Schneider, C. A., Rasband, W. S., & Eliceiri, K. W. (2012). NIH Image to ImageJ: 25 years of image analysis. Nature methods, 9(7), 671.

Schouwstra, R., De Vaux, D., Hey, P., Malysiak, V., Shackleton, N., Bramdeo, S. (2010). Understanding Gamsberg–A geometallurgical study of a large stratiform zinc deposit. Minerals Engineering, 23(11-13), 960-967.

Simonetti, A. (2012). Data reduction protocols - Isotope ratio measurements [Powerpoint slides]. Obtained from: https://www3.nd.edu/∼asimonet/ENGV60500/FALL2012/LECTURES_PDFs/LECTURE_9_DRProtocols_10_30_2012.pdf at 24-5-2018

Spry, P. G., Teale, G. S., & Steadman, J. A. (2009, May). Classification of Broken Hill-Type Pb-Zn-Ag Deposits: A Refinement. In AGU Spring Meeting Abstracts.

Stalder, M., Rozendaal, A. (2004) Apatite nodules as an indicator of depositional environment and ore genesis for the Mesoproterozoic Broken Hill- type Gamsberg Zn- Pb deposit,

Namaqua Province, South Africa. Mineralium Deposita, 39 (2), pp. 189-203.

Stalder, M., & Rozendaal, A. (2005). Distribution and geochemical characteristics of barite and barium-rich rocks associated with the Broken Hill-type Gamsberg Zn-Pb deposit, Namaqua Province, South Africa. South African Journal of Geology, 108(1), 35-50.

Strauss, H. (1997). The isotopic composition of sedimentary sulfur through time. Palaeogeography, Palaeoclimatology, Palaeoecology, 132(1-4), 97-118.

Thode, H. G. (1970).Sulfur isotope geochemistry and fractionation between coexisting sulfide minerals. Mineralogical Society Of America Special Paper Number Three, 133-144

Thode, H. G. (1991). Sulphur isotopes in nature and the environment: an overview. Stable isotopes: natural and anthropogenic sulphur in the environment, 43, 1-26.

Thomas, R. J., Von Veh, M. W., & McCourt, S. (1993). The tectonic evolution of southern Africa: an overview. Journal of African Earth Sciences (and the Middle East), 16(1-2), 5-24.

Thomas, R. J., Agenbacht, A. L. D., Cornell, D. H., & Moore, J. M. (1994). The Kibaran of southern Africa: tectonic evolution and metallogeny. Ore Geology Reviews, 9(2), 131-160.

Tikkanen, G. D. (1986). World resources and supply of lead and zinc. Economics of internationally traded minerals. Littleton, CO, Soc. Min. Eng, 242-250.

Vedanta Zinc International (2018) Creating a world-class Zinc complex. https://www.vedanta-zincinternational.com/downloads/send/22-2018/108-creating-a-world-class-zinc-complex, retrieved 16 March 2018

Von Gehlen K, Nielsen H, Chunnett I, Rozendaal A. (1983). Sulfur isotopes in metamorphosed Precambrian Fe-Pb-Zn-Cu sulfides and barite at Aggeneys and Gamsberg. Mineralogical Magazine, South Africa, 47:481–486

Widdel F. & Hansen T. A. (1992) The dissimilatory sulfate- and sulfur-reducing bacteria. In The Prokaryotes (ed. A. Barlows et al.), pp. 583-624, Springer Verlag.

Willner, A. P. (1995). Pressure-temperature evolution of a low-pressure amphibolite facies terrane in central Bushmanland (Namaqua mobile belt, South Africa). Communications of the geological Survey of Namibia, 10, 5-19.